

Oh Boi Its my Thesis

by

Anna Maria Houk

A thesis
presented to the University of Waterloo
in fulfillment of the
thesis requirement for the degree of
Masters of Science
in
Electrical and Computer Engineering - Quantum Information

Waterloo, Ontario, Canada, 2022

© 2022

Author's Declaration

I hereby declare that I am the sole author of this thesis. This is a true copy of the thesis, including any required final revisions, as accepted by my examiners.

I understand that my thesis may be made electronically available to the public.

Abstract

This is the abstract.

Acknowledgements

.

Dedication

.

Table of Contents

List of Figures	viii
List of Tables	xi
1 Introduction	1
1.1 Motivation	1
1.2 Thesis Outline	1
2 Background	2
2.1 Hollow-Core Photonic Crystal Fiber	2
2.1.1 Conventional TIR Guidance	2
2.1.2 Photonic Crystal Bandgap	2
2.1.3 Bandgap Shift	10
3 Liquid-Filled HCPCF	12
3.1 Filling Methods	12
3.2 Experimental Set-Up	14
3.3 H ₂ O and D ₂ O Transmission	14
3.4 Results	16
3.4.1 Selective Filling	16
3.4.2 Full-Fiber Filling	18

3.5	Carbon Nanotubes	19
3.5.1	Characterizing Carbon Nanotubes	19
3.5.2	Nonlinear Optical Properties of CNTs	25
3.5.3	Fluorescence of CNTs	26
4	Optical Excitation of Semiconductor Nanoparticles in Hollow-Core Fiber	29
4.1	Bandgap Overlap	29
4.1.1	Particle-Mode Interaction and Optical Depth	31
4.2	Indocyanine Green	32
4.2.1	Experiment Set-Up	38
4.2.2	ICG in HCPCF	38
5	Conclusion	43
5.0.1	Experimental Outcomes	43
5.1	ECDL	44
	References	45
	APPENDICES	49
.1	CNT Sample Preparation	49
	Glossary	50
	Abbreviations	51
	Nomenclature	52
	List of Symbols	53

List of Figures

2.1	(a)cross-section of HCPCF highlighting the PC pattern (b)reduced to 1-dimension (2)in 2-dimensions	3
2.2	Band plot for a 1D photonic crystal with parameters-, -, solved using Finite Difference Time Domain(FDTD) method[4].	6
2.3	(a) primitive lattice vectors and (b) primitive reciprocal lattice vectors with first Brillouin zone (green) and irreducible Brillouin zone (red) depicted for a honeycomb lattice structure.	7
2.4	Band plot along the irreducible Brillouin zone for a honeycomb lattice with parameters -, -, . Solved for using Plane Wave Expansion(PWE) numerical method[4].	9
3.1	Side profile of collapsed cladding 1550HC fiber running the fiber splicer with varying current strength and duration.	13
3.2	Variation between fibers using splicer settings 70ms 25ms	13
3.3	Fiber transmission experimental set-up.	14
3.4	The transmission of heavy water(green) and regular water(blue) is shown for slabs of thickness ranging from 1cm to 8cm in increments of 1cm using absorption data recorded by [10].	15
3.5	Transmission of H ₂ O and D ₂ O in (a)selectively-filled 800nm hollow-core fiber.	17
3.6	Modeshape of 1550 hollow-core fiber filled with (a)air (b)heavy water (c)distilled water. Fiber filled with heavy water maintains a Gaussian profile while the fiber with regular distilled water shows some distortion.	18
3.7	Transmission of H ₂ O and D ₂ O in fully-filled 1550nm hollow-core fiber.	18

3.8	REPLACE Chiralities of CNTs with red dots indicating metallic and open dots [11].	21
3.9	REPLACE Bands for (a)(c)Metallic and (b)(d)Semiconducting CNTs and their energy band gaps [13]	22
3.10	Chiralities of CNTs with red dots indicating metallic and open dots Calculated gap energies between mirror-image spikes in density of states for $\gamma = 2.75$ eV. For (solid circles) metallic and (open circles) semiconducting, and (double circles) armchair CNTs. [16].	24
3.11	Group characteristics of CNTs colored by (a)chiral angle and (b)diameter	28
4.1	Hollow-core fiber bandgap overlayed on CNT emission vs. excitation wavelengths	30
4.2	1550HC CNTs	30
4.3	(a) Depiction of the Homo-Lumo gap in organic semiconductors and the transition occurring between ground and excited states. (b) The chemical structure of ICG provided by MP Biomedicals.	32
4.4	Absorption cross-section at peak wavelengths 700nm(blue) and 780nm(green) for ICG dissolved in D2O(a) and H2O(b) . Data from (cite) was fitted using a linear regression model.	33
4.5	Degradation of a 4.5ppm initial concentration sample after 4hrs of light exposure reduced to a 2ppm concentration.	36
4.6	(a)Fluoresce spectrum of 4.5ppm sample (b) Maximum fluorescence and maximum absorption spectrum of 4.5ppm initial concentration sample . . .	37
4.7	Absorption spectrum of ICG samples (a) 2.5 ppm concentration in core of 800nm HCPCF and (b) 4 ppm concentration in core and cladding of 1550nm HCPCF.	38
4.8	(a) The maximum fraction of fluorescence is plotted against excitation wavelength for a 4ppm ICG sample in a 1cm piece of 1550nm HCPCF and 1cm cuvette. The maximum fraction of fluorescence of the ICG in the cuvette is only 4% of that measured in fiber. (b) The optical density at each excitation wavelength. The fraction of fluorescence spectrum of the 4ppm ICG solution in (c) 1550nm HCPCF (d) a cuvette.	40

4.9	Measurements of 3.7ppm ICG sample in a 2cm piece of core-filled 800nm HCPCF (a) The maximum fraction of fluorescence and optical density against excitation wavelength. (b) The fraction of fluorescence spectrum (c) Measured output peak power and fractional fluorescence as a function of input power.	41
5.1	(a) (b)	43

List of Tables

4.1	Thorlabs fiber bandgap shift.	29
4.2	CNTs with emission and excitation transmittable through HC1550 filled with D ₂ O.	30
4.3	Absorption Cross Section parameter fitting of ICG dissolved in deionized water. Fitting done with linear regression on σ vs. concentration data measured at $\lambda = 780nm$ from literature.	35
4.4	Absorption Cross Section parameter fitting of ICG dissolved in deionized water. Fitting done with linear regression on σ vs. concentration data at $\lambda = 700nm$ from literature.	35
4.5	Absorption Cross Section parameter fitting of ICG dissolved in heavy water. Fitting done with linear regression on σ vs. concentration data at $\lambda = 700nm$ from literature.	35

Chapter 1

Introduction

In the beginning, there was π :

$$e^{\pi i} + 1 = 0 \tag{1.1}$$

A [computer](#) could compute π all day long. In fact, subsets of digits of π 's decimal approximation would make a good source for psuedo-random vectors, [v](#) .

1.1 Motivation

See equation [1.1](#) on page [1](#).¹

1.2 Thesis Outline

The credo of the [American Association of Amateur Astronomers and Zoologists \(AAAAZ\)](#) was, for several years, several paragraphs of gibberish, until the [dingledorf](#) responsible for the [AAAAZ](#) Web site realized his mistake:

¹A famous equation.

Chapter 2

Background

2.1 Hollow-Core Photonic Crystal Fiber

2.1.1 Conventional TIR Guidance

2.1.2 Photonic Crystal Bandgap

The 1D and 2D views of the structure

A periodic non-magnetic medium will have repeating dielectric constant[?]

$$\varepsilon(\mathbf{r}) = \varepsilon(\mathbf{r} + \mathbf{a}) \quad (2.1)$$

Due to its discrete and invariant translation symmetry, the dielectric constant along the medium can be expanded as a Fourier series

$$\varepsilon(\mathbf{r}) = \sum_{\mathbf{G}} \varepsilon_{\mathbf{G}} e^{i\mathbf{G} \cdot \mathbf{r}} \quad (2.2)$$

Where \mathbf{G} are the reciprocal lattice vectors such that $\mathbf{G} \cdot \mathbf{a} = 2\pi n$. Expressing the electric field also as a Fourier integral

$$\mathbf{E}(\mathbf{r}) = \iiint d^3\mathbf{k} \mathbf{A}(\mathbf{k}) e^{i\mathbf{k} \cdot \mathbf{r}} \quad (2.3)$$

Using the Maxwell equations (2.4) the wave equation can be written in terms of the electric field

$$\begin{cases} \vec{\nabla} \times \vec{H} &= -i\omega\epsilon(\vec{r})\vec{E} \\ \vec{\nabla} \times \vec{E} &= i\omega\mu_0\vec{H} \end{cases} \quad (2.4)$$

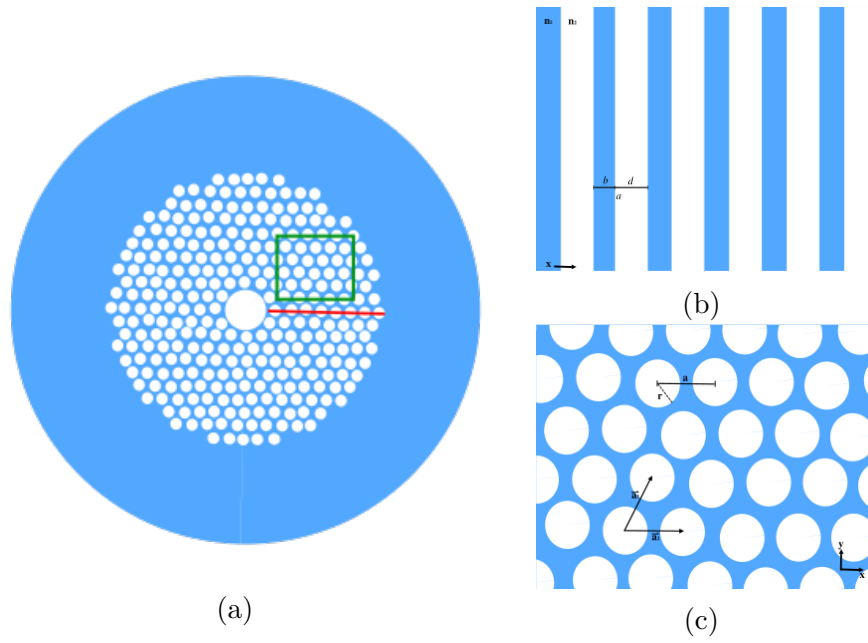


Figure 2.1: (a)cross-section of HCPCF highlighting the PC pattern (b)reduced to 1-dimension (2)in 2-dimensions

$$\nabla \times (\nabla \times \mathbf{E}) - \omega^2 \varepsilon(\mathbf{r}) \mu_0 \mathbf{E} = 0 \quad (2.5)$$

Substituting (2.2) and (2.3) into the above results in the dispersion relation:

$$\mathbf{k} \times (\mathbf{k} \times \mathbf{A}(\mathbf{k})) + \omega^2 \mu_0 \sum_{\mathbf{G}} \varepsilon_{\mathbf{G}} \mathbf{A}(\mathbf{k} - \mathbf{G}) = 0 \quad (2.6)$$

in where for any vector \mathbf{K} the solutions of (2.6) for the coefficient $\mathbf{A}(\mathbf{K})$ are grouped with the coefficients $\mathbf{A}(\mathbf{K} - \mathbf{G})$, decoupling the coefficients of other vectors that cannot be expressed in the form $\mathbf{K} - \mathbf{G}$. Disregarding the decoupled vectors, the total electric field can be described as a superposition of normal modes with regard to a chosen vector \mathbf{K} :

$$\mathbf{E}_{\mathbf{k}}(\mathbf{r}) = \sum_{\mathbf{G}} \mathbf{A}(\mathbf{K} - \mathbf{G}) e^{i(\mathbf{k} - \mathbf{G}) \cdot \mathbf{r}} \quad (2.7)$$

we can pull out the Bloch theorem for the electric field from (2.7)

$$\mathbf{E}_{\mathbf{k}}(\mathbf{r} + \mathbf{a}) = e^{i\mathbf{k} \cdot \mathbf{a}} \mathbf{E}_{\mathbf{k}}(\mathbf{r}) \quad (2.8)$$

$$\mathbf{u}_{\mathbf{k}}(\mathbf{r}) = \sum_{\mathbf{G}} \varepsilon_{\mathbf{G}} e^{i\mathbf{G} \cdot \mathbf{r}} \quad (2.9)$$

$$\varepsilon_{\mathbf{G}} = \frac{1}{V} \int d^3r e^{-i\mathbf{G} \cdot \mathbf{r}} \mathbf{u}_{\mathbf{k}}(\mathbf{r}) \quad (2.10)$$

(Expand) Returning to (2.6), can fix ω to find the corresponding \mathbf{K} and normal modes of the system. However, in the case of photonic crystals there are ranges of frequencies that have no \mathbf{K} s with real solutions, which implies that waves of these frequencies cannot propagate through the photonic crystal. These non-propagating frequencies are referred to as the photonic band gap.

1D Photonic Bandgap

Returning to the 1D periodic stack pictured in ?? the periodicity of dielectric constant is described by $\varepsilon(z) = \varepsilon(z + p)$ where $a = b + d$, the length of one period. The reciprocal lattice vector will be $\mathbf{G}_n = n \frac{2\pi}{a} \hat{z}$ and plugging into the Fourier series expansion of $\varepsilon(z)$ from (2.2)

$$\varepsilon(z) = \sum_{n=-\infty}^{\infty} \varepsilon_n e^{in \frac{2\pi}{a} \hat{z}} \quad (2.11)$$

From the reduction to propagation in the z-direction with the electric field oriented in x-direction, (2.6) simplifies

$$K^2 A(K) + \omega^2 \mu_0 \sum_{n=-i\infty}^{\infty} \varepsilon_n A(K - n \frac{2\pi}{a}) = 0 \quad (2.12)$$

Expanding the Fourier coefficients to the 1st order and reducing the equations to the dominant coefficients of the form $A(K)$ and $A(K - \frac{2\pi}{a})$. $|K - g| = K$ and $K = \frac{\pi}{a}$ gives a system of equations that can be solved to find the dispersion relation $\omega(K)$.

$$\begin{cases} (K^2 - \omega^2 \mu_0 \varepsilon_{00}) A(K) = \omega^2 \mu_0 \varepsilon_1 A(K - g) \\ \omega^2 \mu_0 \varepsilon_{-1} A(K) = ((K - g)^2 - \omega^2 \mu_0 \varepsilon_{00}) A(K - g) \end{cases} \quad (2.13)$$

The equations relating these two modes has a solution at

$$(K^2 - \omega^2 \mu_0 \varepsilon_{00})((K - g)^2 - \omega^2 \mu_0 \varepsilon_{00}) - (\omega^2 \mu_0 \varepsilon_1)(\omega^2 \mu_0 \varepsilon_{-1}) = 0 \quad (2.14)$$

noting $\varepsilon_1 = \varepsilon_{-1}^*$ and $K \approx 2g$ simplifies the relationship

$$\omega_{\pm}^2 = \frac{K^2}{\mu_0(\varepsilon_{00} \mp |\varepsilon_1|)} \quad (2.15)$$

The dispersion relation has two possible solutions, which specify the top and bottom of the photonic bandgap edges, as illustrated in 2.2 If the solving for the wavevector at a frequency between ω_{\pm} , only complex solutions will exist. This means that only evanescent waves, not electromagnetic waves, propagate through the medium while the electromagnetic waves are reflected back; the medium acts as a mirror for the bandgap wavelengths.

This is the the phenomena that allows for HCPCF to guide certain frequencies of light - wavelengths in the bandgap are reflected by surrounding Bragg Grating confining them to the core of the fiber, while the rest are allowed to propagate through the grating.

2D Photonic Bandgap

To understand the full picture of light propagation in hollow-core fiber, we need to expand to the 2D case pictured in 2.1c. However, with the electromagnetic waves now propagating in two dimension there is an added layer of complexity with the TE TM wave polarizations and the bandgaps. In addition to controlling the refractive index of the material and the period of the lattice, the lattice structure and hole radius will affect the performance of the

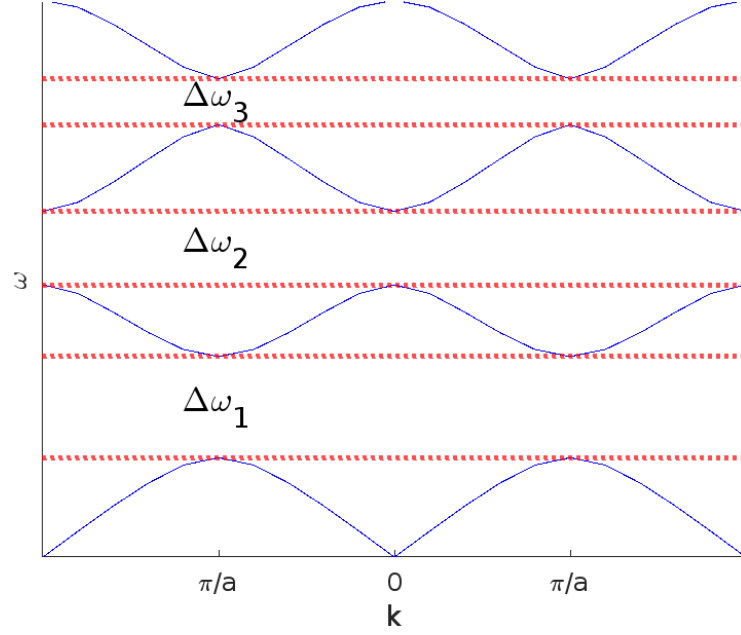


Figure 2.2: Band plot for a 1D photonic crystal with parameters-, τ -, solved using Finite Difference Time Domain(FDTD) method[4].

photonic crystal, the latter playing a large role in the completeness of the photonic bandgap. In the 2D photonic crystal, the in-plane guided modes will have either magnetic fields in-plane and electric fields perpendicular to the lattice (TE modes) or electric fields in-plane and magnetic fields perpendicular to the lattice (TM modes). As the TE and TM modes are perpendicular to each other they may exhibit wildly different dispersion relations, which means that an optical bandgap is not guaranteed to persist for all polarizations[2]. This is certainly the case for square lattice photonic crystals, but other patterns such as the honeycomb (which is the structure in our HCPCF) do have a bandgap persisting for all all polarizations[3]. This all to say, it is important to consider all polarization effects when making decisions about photonic crystal patterns for two or more dimensions.

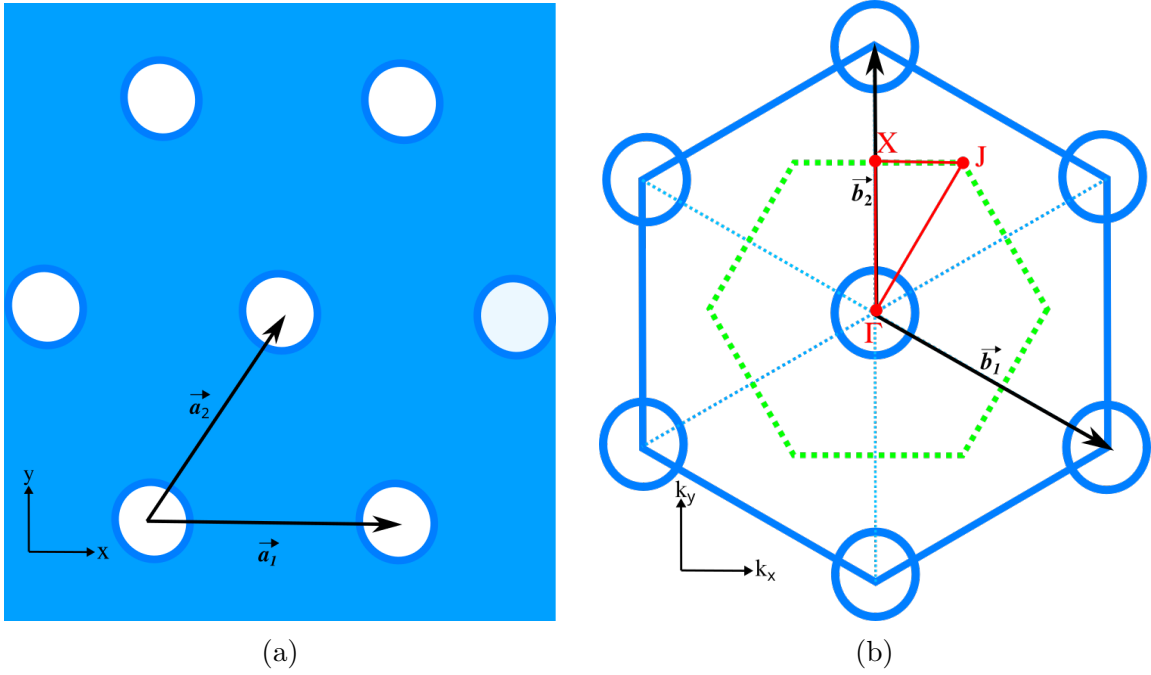


Figure 2.3: (a) primitive lattice vectors and (b) primitive reciprocal lattice vectors with first Brillouin zone (green) and irreducible Brillouin zone (red) depicted for a honeycomb lattice structure.

Considering the lattice structure in 2.3(a), and taking propagation in the xy-plane ($K_z = 0$ and $z = 0$ for simplicity), the wavevector and position vectors reduce to $\mathbf{K}_{||} = k_x \hat{x} + k_y \hat{y}$ and $\mathbf{r}_{||} = x \hat{x} + y \hat{y}$. The primitive lattice vectors of a honeycomb photonic crystal will be:

$$\mathbf{a}_1 = a \hat{x} \quad \mathbf{a}_2 = \frac{a}{2} \hat{x} + \frac{a\sqrt{3}}{2} \hat{y} \quad (2.16)$$

and transforming to the momentum-space, $\mathbf{b} \cdot \mathbf{a} = 2\pi\delta_{ij}$, as shown in 2.3(b) the primitive reciprocal lattice vectors are

$$\mathbf{b}_1 = \frac{2\pi}{a} \hat{x} - \frac{2\pi}{a\sqrt{3}} \hat{y} \quad \mathbf{b}_2 = \frac{4\pi}{a\sqrt{3}} \hat{y} \quad (2.17)$$

Taking these in combination of n, m integer scaling factors, the reciprocal lattice vector is defined $\mathbf{G}_{||} = n\mathbf{b}_1 + m\mathbf{b}_2$. The electromagnetic field defined for a two dimensional system

$$\mathbf{E}(\mathbf{r}) = e^{i\mathbf{k} \cdot \mathbf{r}} \sum_{m=-\infty}^{\infty} \sum_{n=-\infty}^{\infty} \mathbf{E}_{m,n} e^{i(n\mathbf{b}_1 + m\mathbf{b}_2) \cdot \mathbf{r}} \quad (2.18)$$

and the correlating Fourier expansion of dielectric function (2.10)

$$\varepsilon_{\mathbf{G}_{||}} = \frac{1}{a' \cdot b'} \int dx dy e^{i(G_x x + G_y y)} \mathbf{u}_{\mathbf{k}}(x, y) \quad (2.19)$$

are substituted into (2.4). Utilizing the lattice symmetry and periodicity, the problem can be restricted to only solve for Bloch modes inside the of the irreducible Brillouin zone. The first Brillouin zone is defined by the perpendicular bisectors to the primitive reciprocal lattice vectors, depicted in green in 2.3(b) and can be further subdivided into the irreducible Brillouin zone shown in red. In order to find the photonic bandgap, solving the dispersion equation just along the irreducible Brillouin zone is sufficient. For a honeycomb lattice, the k -path to follow would be

$$\begin{cases} |\Gamma X| = \frac{2\pi}{a\sqrt{3}}, & k_x = 0, 0 < k_y < \frac{2\pi}{\sqrt{3}a} \\ |XJ| = \frac{2\pi}{3a}, & 0 < k_x < \frac{2\pi}{3a}, k_y = \frac{2\pi}{\sqrt{3}a} \\ |\Gamma J| = \frac{4\pi}{3a}, & 0 < k_x < \frac{2\pi}{3a}, k_y = \sqrt{3}k_x \end{cases} \quad (2.20)$$

Discretizing 2.18 and 2.19 then picking a few points along the k -path, numerical methods can be used to solve for the optical bandgap. 2.4 shows the resulting TE bandgap for a honeycomb lattice with parameters-, -, using Plane Wave Expansion(PWE)[4].

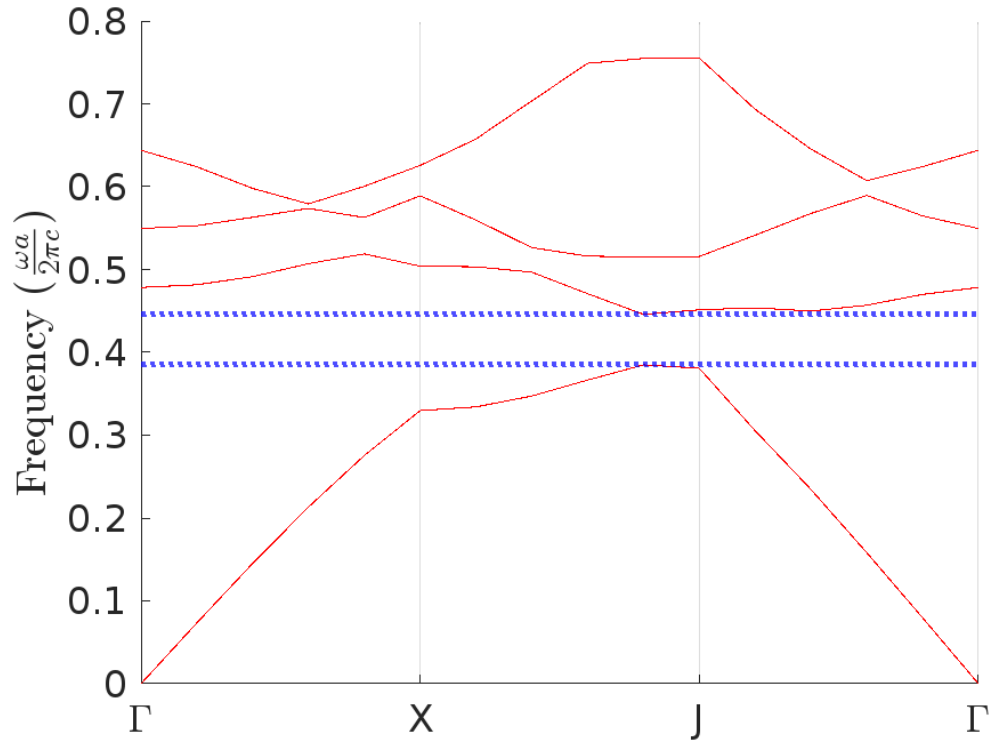


Figure 2.4: Band plot along the irreducible Brillouin zone for a honeycomb lattice with parameters a, c, ϵ . Solved for using Plane Wave Expansion(PWE) numerical method[4].

2.1.3 Bandgap Shift

modal magnetic field distributions satisfy:

$$(\nabla_t^2 + k^2 n(\mathbf{r})^2 - \beta) \mathbf{H}(\mathbf{r}) = (\nabla_t \times \mathbf{H}(\mathbf{r})) \times (\nabla_t \ln(n(\mathbf{r})^2)) \quad (2.21)$$

gives scaling law for absolute refractive index at fixed contrast "a solution for a transverse scale represented by Λ is replicated in an identical structure with a different Λ if the wavelength is scaled proportionately, to keep $k\Lambda$ constant"

"We emphasise that the scalar wave equation (and therefore the scaling laws derived from it) is accurate for the smallest index contrasts only. However, for step-index structures the vector term in Eq. (2) only exists at boundaries, so the scalar wave equation accurately represents wave propagation elsewhere. Since bandgaps arise from interference and resonance effects among such generic waves, the scaling laws of Eq. (5) should be at least approximately valid" 1.45 RI contrast[5]

Scaling law for the wave equation for the transverse coordinates $X = x\Lambda^{-1}$ $Y = y\Lambda^{-1}$ where Λ is a solution to the transverse scale.

$$n(X, Y) = \begin{cases} 1, & n_1 \text{ (high RI)} \\ 0, & n_2 \text{ (low RI)} \end{cases} \quad (2.22)$$

normalized scaled wave equation:

$$\nabla_{\perp}^2 \Psi + (v^2 n(X, Y) - w^2) \Psi = 0 \quad (2.23)$$

With $\nabla_{\perp} = \partial^2/\partial X^2 + \partial^2/\partial Y^2$ solving for the frequency parameter v^2 and eigenvalue w^2 :

$$\begin{aligned} v^2 &= \Lambda^2 k^2 (n_1^2 - n_2^2) \\ w^2 &= \Lambda^2 (\beta^2 - k^2 n_2^2) \end{aligned} \quad (2.24)$$

from the equation above we see that the w^2 is determined by the frequency parameter v^2 and the index distribution function $n(X, Y)$. This implies that w^2 and v^2 are invariant with changes to the parameters k, Λ, n_1, n_2 . $k = \omega/c$ $\beta = k \cos \theta$ longitudinal component of the wavevector. Because the light propagates along the fiber, much of its wavevector is taken up by the longitudinal component.

In the HCPCF case where the glass refractive index is held constant and the air in the fiber is replaced by a new material the equations can be rewritten with $n_1 = n_{glass}$ and $n_2 = n_{air} = 1$:

$$\begin{aligned} v^2 - w^2 &= \Lambda^2 (k^2 n_{glass} - \beta^2) \\ v &= k \Lambda n_{glass} \sqrt{n_{air} - \frac{n_{air}}{n_{new}}} \end{aligned} \quad (2.25)$$

The initial index contrast $N_0 = \frac{n_{air}}{n_{glass}}$ moves to $N = \frac{n_{new}}{n_{glass}}$ with the change in RI $n_{air} < n_{new} < n_{glass}$. This leads to the new center bandgap to be governed by the equation:

$$\lambda = \lambda_0 \sqrt{\frac{1 - N^{-2}}{1 - N_0^{-2}}} \quad (2.26)$$

This has been experimentally confirmed to hold for HCPCF [7].

Chapter 3

Liquid-Filled HCPCF

3.1 Filling Methods

Fibers were cut to between 6cm and 8cm in length. To ensure consistent coupling and positioning, light was coupled to the core of the fiber by connecting to a solid-core PM780HP fiber via a mechanical splicing chip [8]. We replaced the air in 1550nm HCPCF with deionized water and heavy water by utilizing capillary action. To selectively fill the core of 800nm HCPCF, the photonic crystal cladding was collapsed while leaving the hollow-core open and is similarly filled with liquid using capillary action. We collapsed the cladding by placing the HCPCF opposite of a solid-core fiber in a fusion splicer [9] and adjusting arc current duration and power to melt the cladding structure while remaining distanced enough to prevent fusion with the solid-core fiber.

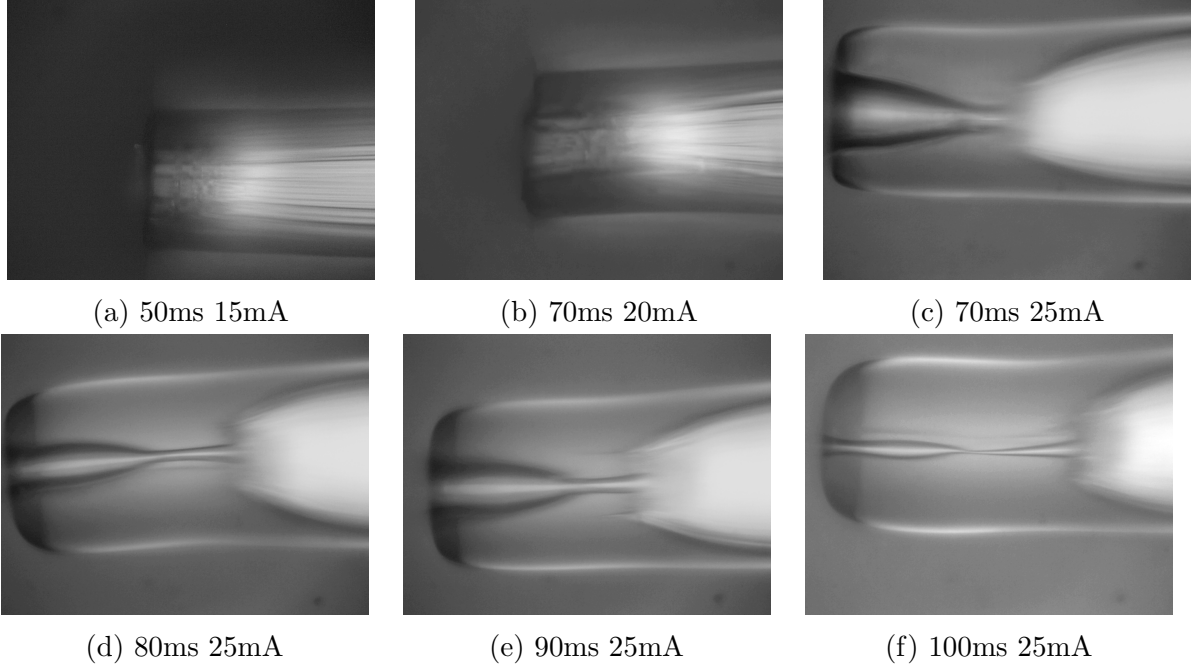


Figure 3.1: Side profile of collapsed cladding 1550HC fiber running the fiber splicer with varying current strength and duration.

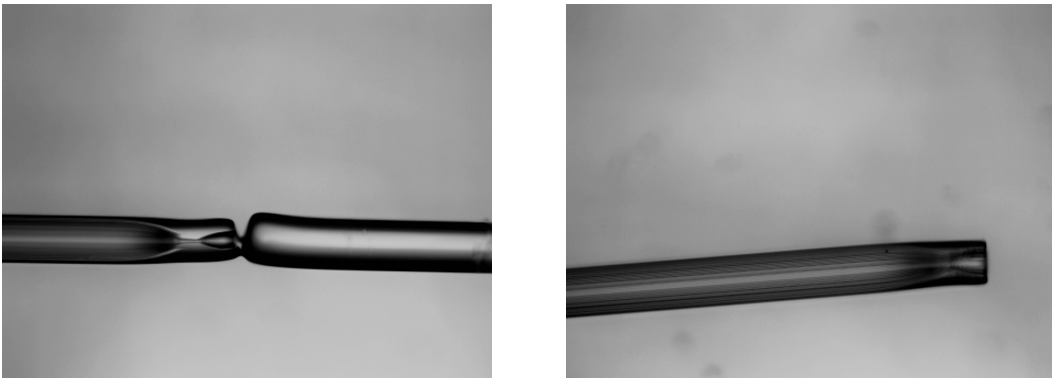


Figure 3.2: Variation between fibers using splicer settings 70ms 25ms

3.2 Experimental Set-Up

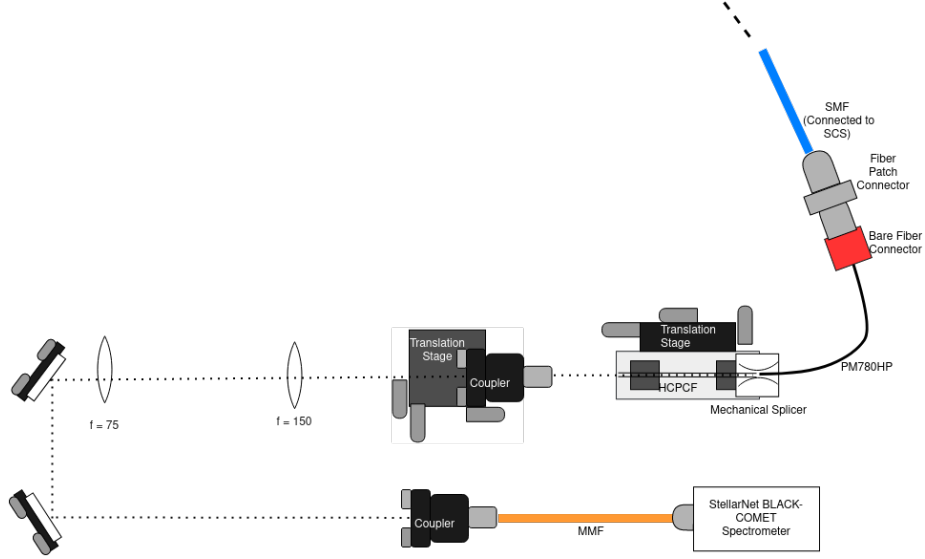


Figure 3.3: Fiber transmission experimental set-up.

3.3 H_2O and D_2O Transmission

HCPCF uses a photonic crystal cladding composed of a periodic silica structure that allows light to be guided through a hollow and thus low-refractive index core. In some applications of HCPCF, such as fiber-integrated sensors and on-linear optics, the hollow regions of the fiber are filled with liquids or gasses. Fibers that are fully-filled with water will produce a frequency shift in the bandgap due to refractive index scaling[7]. On the other hand, when the core is selectively filled with water, light will be guided via total-internal reflection. We investigate the transmission spectra of fully-filled and core-filled fibers for deionized water and heavy water.

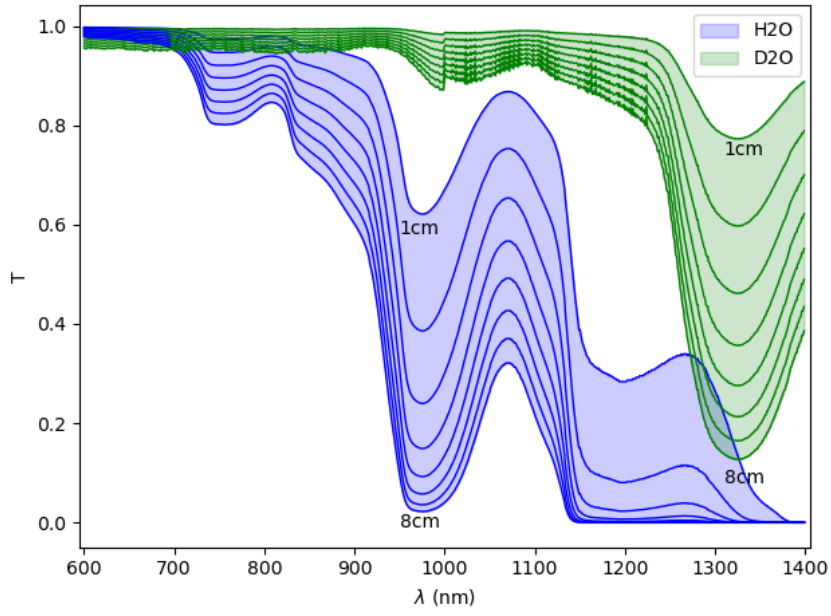


Figure 3.4: The transmission of heavy water(green) and regular water(blue) is shown for slabs of thickness ranging from 1cm to 8cm in increments of 1cm using absorption data recorded by [10].

3.4 Results

The air-filled 800nm HCPCF covers a transmission spectral range of 750nm–950nm. Light exits the fiber with a Gaussian mode shape and has an expected coupling between 75-80% when connected to a solid-core single-mode fiber. A water-filled core retains a Gaussian mode shape and has a 30% reduction in the normalized transmission for wavelengths above 850nm, which is consistent with the absorption spectrum of H₂O [10]. We also observe that the coupling efficiency of the fiber drops to 31%. With a heavy water filled core, there are no significant changes in the normalized transmission spectrum, minimal effects to the absorption over this region, and coupling efficiency of up to 67%.

The air-filled 1550nm HCPCF covers a transmission spectral range of 1200nm–1700nm. With a filled core and cladding, the spectral range shifts to transmitting wavelengths between 600nm–1100nm for both heavy water and water, which aligns with the scaling laws prediction. Heavy water achieved a coupling efficiency of 47%, but water only 16%. The existing mode shape is roughly Gaussian but contains noise as some light also leaks from the photonic structure, worse for water than heavy water. The losses seen in water are not entirely explained, but losses and effects from the decrease in refractive index contrast are also present in the D₂O-filled fiber. While there is a less than 20% difference in absorption coefficient between the 550nm–830nm for the fiber length, 7.6nm, between 830nm–950nm the absorption coefficient of water increases steeply but stays constant over the same region for heavy water.

3.4.1 Selective Filling

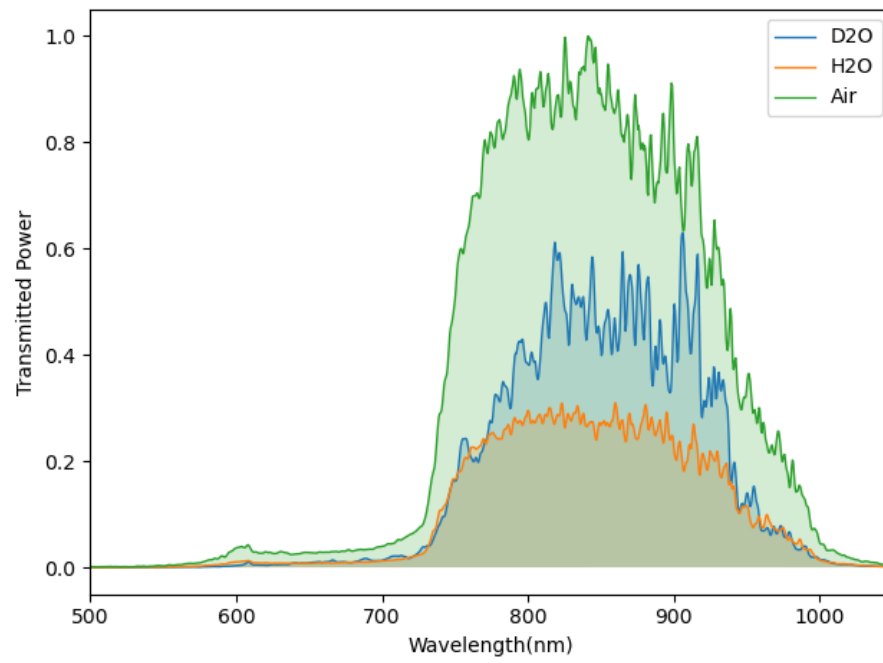


Figure 3.5: Transmission of H₂O and D₂O in (a)selectively-filled 800nm hollow-core fiber.

3.4.2 Full-Fiber Filling

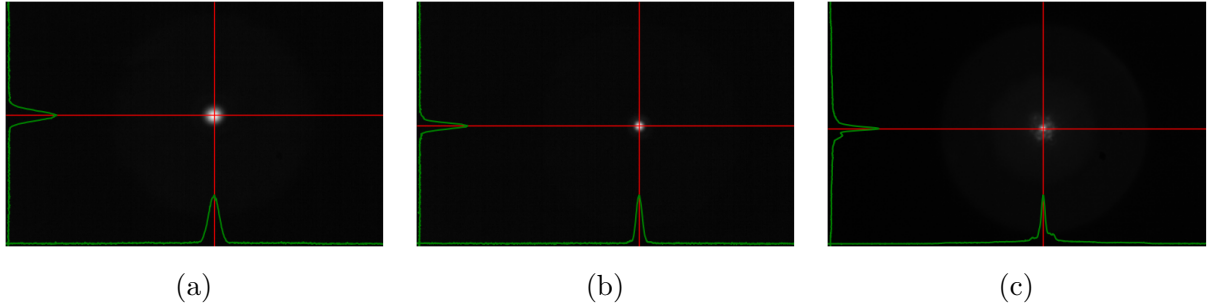


Figure 3.6: Modeshape of 1550 hollow-core fiber filled with (a)air (b)heavy water (c)distilled water. Fiber filled with heavy water maintains a Gaussian profile while the fiber with regular distilled water shows some distortion.

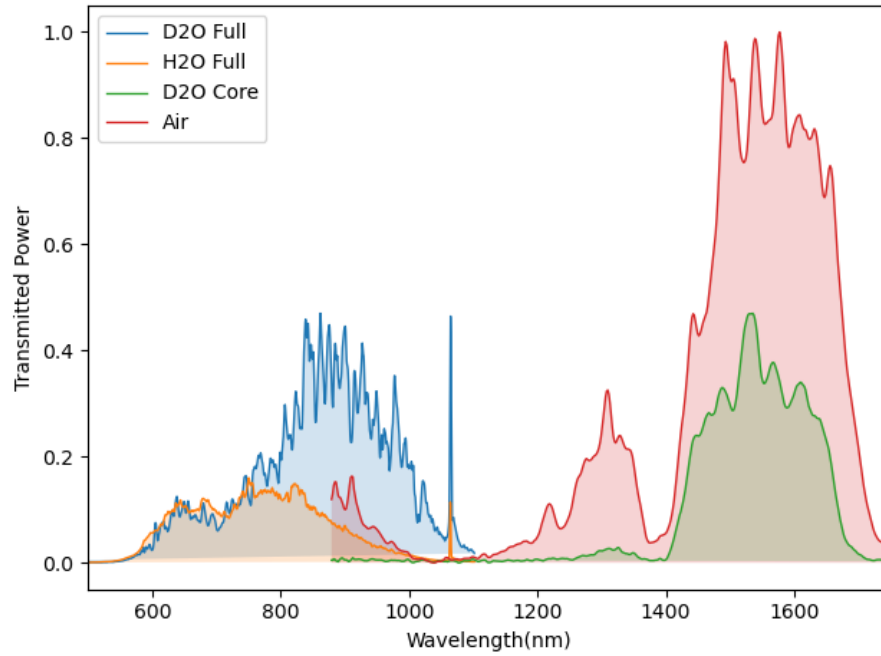


Figure 3.7: Transmission of H_2O and D_2O in fully-filled 1550nm hollow-core fiber.

3.5 Carbon Nanotubes

First discovered by S.Iijima and T. Ichihashi in 1993, carbon nanotubes (CNT) are single layers of graphene rolled up into a hollow cylinder near 1 nm in diameter and near 1 μ m in length. While graphene is a 2-dimensional material, the dimensions of CNTs allow them to be treated as 1-dimensional materials.

3.5.1 Characterizing Carbon Nanotubes

The main descriptive properties of CNTs are the chiral vector, which is a scaled integer-valued combination of the unit vectors for the honeycomb structure of graphene, written in the form (n, m) .

$$C_h = na_1 + ma_2 = (n, m) \quad (3.1)$$

The unit vectors in Cartesian coordinates are

$$a_1 = \left(\frac{\sqrt{3}}{2}, \frac{1}{2}\right)\sqrt{3}a_{C-C}, a_2 = \left(\frac{\sqrt{3}}{2}, -\frac{1}{2}\right)\sqrt{3}a_{C-C} \quad (3.2)$$

and have equal length a_{C-C} , where a_{C-C} is the length of the carbon bond, which for graphene is 1.421 (Å), and often approximated as 1.44 (Å) for CNTs, though there is variation depending on the curvature of the nanotubes[14]. The chiral vector is of high value as it reveals a lot of information about the electronic and optical properties of individual CNTs. The chiral angle, the angle between the unit vectors, gives the direction of the chiral vector and is defined as

$$\theta = \tan^{-1} \left[\frac{m\sqrt{3}}{m + 2n} \right] \quad (3.3)$$

and the diameter of a nanotube as

$$d_t = \frac{a_{C-C}\sqrt{3}}{\pi} \sqrt{n^2 + nm + m^2} \quad (3.4)$$

Due to the geometry of graphene, CNTs have a six-fold rotational symmetry and the connection points of the lattice, i.e. the way that the graphene is rolled into a tube will produce equivalent CNTs between n and $n+6$, thus the tube geometries are often constrained to the first range. Nanotubes with a chiral angle of 0° are called zigzag tubes and chiral angles of $\pm 30^\circ$ are called armchair tubes due to the pattern made by their circumference as shown in the Figure 2, and are the two configurations in which CNTs are anti chiral, meaning that their

structures are indistinguishable from their mirrored image, while all in between-angled nanotubes are chiral, i.e. distinguishable from their mirrored image. The diameter and angle actually vary the electronic band structure of the CNT significantly. CNTs have an additional electron confinement around their circumference[13] and as can be seen from the above definitions, the tube diameter of CNTs is quantized and varies depending on how the graphene honeycomb lattice is cut, will also follow the boundary condition

$$C_h \cdot \kappa = 2\pi q \quad (3.5)$$

where C_h is the cutting line along graphene and q is an integer number. Depending on where graphene energy bands are along the cutting line, the corresponding CNT will become metallic or a semiconductor. In Figure 1, the metallic and semiconducting CNTs are mapped out, and a pattern emerges with CNTs with their chiralities — m - n — being a multiple of 3 emerging as metals. Single CNTs exhibit polarization dependence with the electric field in optical selection rules, i.e. the possible transitions from one quantum state to another [15]. The polarization dependence is only strong in zigzag type nanotubes however. The dipole operator in anti chiral tubes will have a parity of -1 in the horizontal plane dipole operator along the z -axis and a +1 parity for dipole vectors along the x , y plane. For z polarized light there is no electronic band transition, while for light polarized perpendicular to the z axis, the angular momentum quantum number can shift by 1. Thus, CNTs will absorb light with the optical polarization parallel to the axial direction of the tube, but in a bundle or grouping of random-oriented CNTs, there will be no polarization dependence.

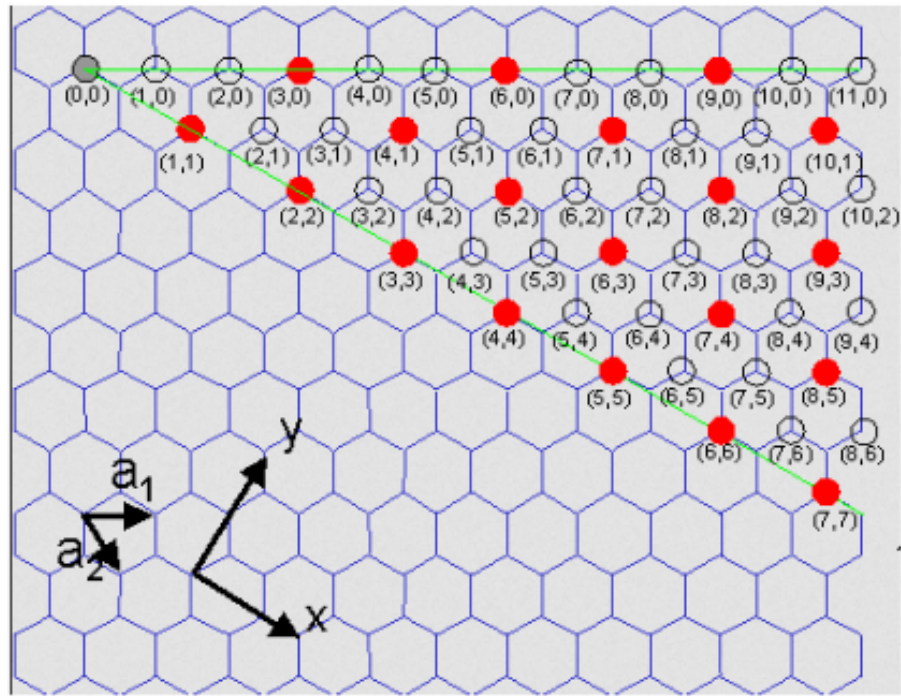


Figure 3.8: REPLACE Chiralities of CNTs with red dots indicating metallic and open dots [11].

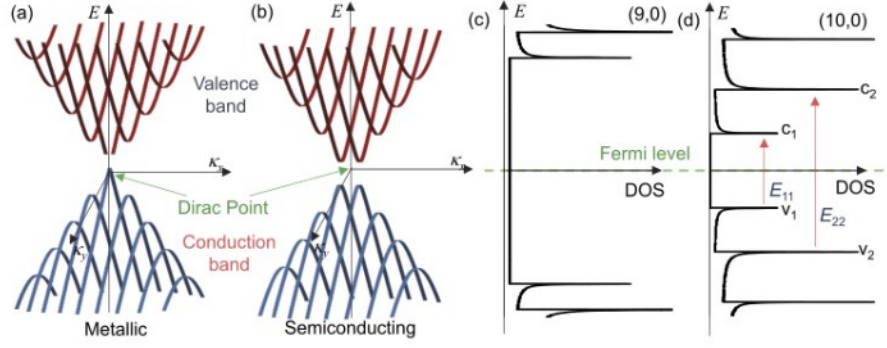


Figure 3.9: REPLACE Bands for (a)(c)Metallic and (b)(d)Semiconducting CNTs and their energy band gaps [13]

In the same year as the emergence of CNTs as a unique material, H. Kataura measured the optical absorption spectra of CNTs of various diameter CNTs performing photothermal deflection spectroscopy, which measures heat produced during relaxation of the electron hole pair generated by the absorbed light [16], an example of the optical absorption spectra are shown in Figure 4. While the absorption spectra across various CNT samples were consistent, the peak positions varied. Using the energy dispersion relations for pi-bands of the graphite [16]

$$E_{2D} = \pm \gamma \sqrt{1 + 4\cos\left(\frac{\sqrt{3}k_x a}{2}\right)\cos\left(\frac{k_y}{2}\right) + 4\cos^2\left(\frac{k_y}{2}\right)} \quad (3.6)$$

where γ is the overall integration and k_x, k_y are the reciprocal lattice vectors, fulfilling the periodic boundary condition for chiral vectors from Eq. (5), the one-dimensional energy band of CNTs could be calculated. Referring to Figure3, the spikes in the DOS correspond to the energy levels of the optical transitions. Plotting the Gap energies from this model against the nanotube diameter in Figure5, referred to commonly as a Kataura plot, shows how the first transition energy of CNTs has a relationship to the diameter by

$$E_{11} = \frac{2\gamma a_{C-C}}{d} \quad (3.7)$$

and the average band gap energies split along semiconductor and metallic chiral values. In short the absorption peak wavelength of a nanotube sample is determined by the mean tube diameter, and the absorption spectral bandwidth will be determined by the tube diameter distribution of the CNT sample.

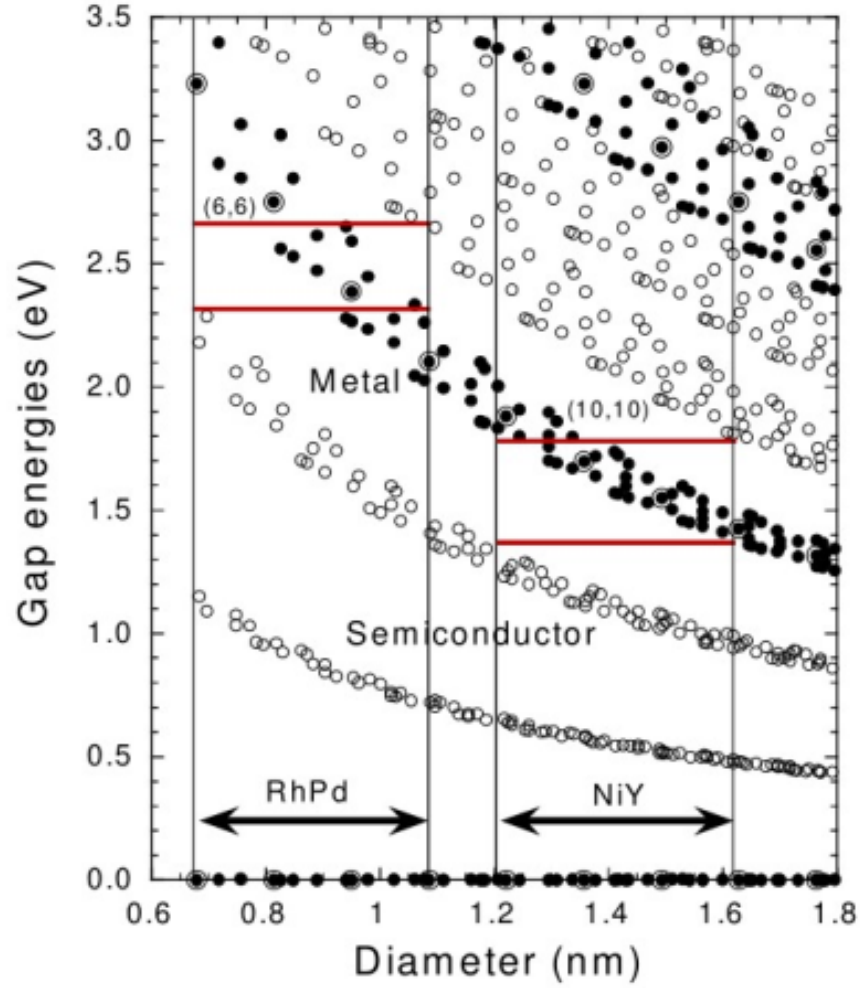


Figure 3.10: Chiralities of CNTs with red dots indicating metallic and open dots Calculated gap energies between mirror-image spikes in density of states for $\gamma = 2.75$ eV. For (solid circles) metallic and (open circles) semiconducting, and (double circles) armchair CNTs. [16].

3.5.2 Nonlinear Optical Properties of CNTs

The general relationship between the polarization and electric field of a material is defined [17] as

$$P(t) = \epsilon_0(\chi^{(1)}E(t) + \chi^{(2)}E^2(t) + \chi^{(3)}E^3(t) + \dots) \quad (3.8)$$

where $\chi^{(1)}$ is the linear susceptibility and $\chi^{(2)}$ and $\chi^{(3)}$ are the second and third order susceptibility. Due to the inversion symmetry of the CNT's structure, the second-order susceptibility is zero. However, a large third-order nonlinearity in CNTs has been measured [22] and is theorized to be a product of the one dimensional motion of the delocalized π -band electrons at a fixed lattice ion configuration [23]. The third-order nonlinearity is responsible for the saturable absorption of a material as well as the nonlinear Kerr effect. The refractive index as defined in Eq.(9) is composed of the real part of the third-order susceptibility with I defining the optical intensity and ω as the optical angular frequency, and is the nonlinear refractive index.

$$n = n_0 + n_2I = n_0 + \frac{3\text{Re}[\chi^{(3)}]}{4\epsilon_0cn_0^2}I \quad (3.9)$$

The absorption coefficient defined by Eq.(9) is composed of the imaginary part of the third-order susceptibility and α_0 , and α_{int} are the linear absorption coefficient, the non saturable absorption coefficient, and refractive index respectively.

$$\alpha = \frac{\alpha_0}{1 + \frac{I}{I_S}} + \alpha_{int} \sim \alpha_0 + \alpha_{int} + \frac{3\omega\text{Im}[\chi^{(3)}]}{2\epsilon_0c^2n_0^2}I \quad (3.10)$$

The saturation intensity, I_S , is the power per unit area it takes in a steady state to reduce the absorption to 1/2 the unbleached (or completely saturated) value and can be written in terms of

$$I_S = \frac{hf}{\sigma\tau} = \frac{E_S}{\tau} \quad (3.11)$$

where σ is the absorption cross section and E_S is the saturation fluence, which is the fluence (i.e. energy per unit area) it takes to reduce the initial fluence value to e^{-1} and τ is the recovery time of the material.

The saturable absorption, as defined by Eq.(11), is a phenomenon where high intensity light will reduce the absorption of a material, but at weak intensity, the light will be absorbed and cause attenuation. This property of materials with strong third-order susceptibility like CNTs can be used to filter out weaker optical signals in noisy optical pulses, while simultaneously allowing strong pulses to pass through. Saturable absorption is observed in all materials with optical absorption resulting from electron transition

between two energy levels [15], but it is rare to find materials that have a recovery time that has a fast recovery time compared to the pulse duration, which in ultra-fast laser applications is in the few picosecond to femtosecond range. The ultra-fast response time of CNTs is only true however for bundles of CNTs with variations in their diameter due to entanglement between semiconducting and metallic via electrons tunneling and coupling from semiconducting CNTs to metallic CNTs [18].

3.5.3 Fluorescence of CNTs

The first Van Hove optical transition (E11) corresponds to the emission frequency and the second Van Hove optical transition (E22) corresponds to the excitation frequency. Equations for first and second van Hoven Transitions optical transition wavelengths as a function of diameter in nanometers and chiral angle are degrees derived in [20], but parameters from [19], which were found by fitting to data of samples of individual SWNT in aqueous sodium dodecyl sulfate (SDS) suspension and are valid for CNT diameters greater than 0.5nm. The parameters differ for each CNT “group”, i.e (n-m) mod 3 = 1 is group 1 (n-m) mod 3 = 2 is group 2 (n-m) mod 3 = 0 are metallic CNTs and do not fluoresce.

Though it is unknown what specific effects contribute to the fitted parameters with the particular samples used, [19]found that other aqueous solutions have comparative spectral shifts of less than 2% compared to the equations when compared to other published results. Comparing to an experimental PL map using a different solution[21], the equation results match quite well (the CNTs present in the left sample are marked in red on the right plot). We can see the expected variation from different solutions, for example CNT (10, 8) has a slightly higher excitation wavelength and slightly lower emission wavelength in SDS than in the NaDDBS/D2O solutions.

Only fully intact and individually dispersed semiconducting CNTs emit fluorescence CNTs coatings or placed on a substrate don’t really fluoresce Interactions between CNTs typically cause quenching effects Though certain materials/solvents (varies with each CNT) can increase fluorescence Isolation is one of the largest factors in quantum yield Only in semiconductor-type CNTs

Desired type of CNTs can be targeted and isolated in a single step using modified aqueous two-phase extraction(ATPS). Hydration modulating agents are mixed in to tune the arrangement of surfactants on their surface

Depending on the mixture, selected CNTs turn highly hydrophobic or hydrophilic

Spectral shift due to the change in the local dielectric environment surrounding CNTs created by solvents and adsorbed molecules.[24]

$$(Emission)\lambda_{11} = \left[\frac{1e7(cm^{-1})}{157.5 + 1066.9d_t} - 771(cm^{-1})\frac{cos(3\theta)^{1.374}}{d_t^{2.272}} \right]^{-1} \quad (3.12)$$

$$(Excitation)\lambda_{22} = \left[\frac{1e7(cm^{-1})}{145.6 + 575.7d_t} + 1326(cm^{-1})\frac{cos(3\theta)^{0.828}}{d_t^{1.809}} \right]^{-1} \quad (3.13)$$

$$(Emission)\lambda_{11} = \left[\frac{1e7(cm^{-1})}{157.5 + 1066.9d_t} + 347(cm^{-1})\frac{cos(3\theta)^{0.886}}{d_t^{2.129}} \right]^{-1} \quad (3.14)$$

$$(Excitation)\lambda_{22} = \left[\frac{1e7(cm^{-1})}{145.6 + 575.7d_t} - 1421(cm^{-1})\frac{cos(3\theta)^{1.110}}{d_t^{2.497}} \right]^{-1} \quad (3.15)$$

Group 1 v. Group 2 Group 1 CNTs have lower Stokes shifts than Group 2 Group 1 have small chiral angles (i 2o) Group 2 span full 0o to 30o chiral angle range, but are grouped along chiral number difference (n - m)

Excitation/Emission wavelengths Increase in Stokes shifts with diameter along chiral difference (n - m) lines Noted in red on lower plot, connected by black lines Increase in ex/em wavelengths with diameter

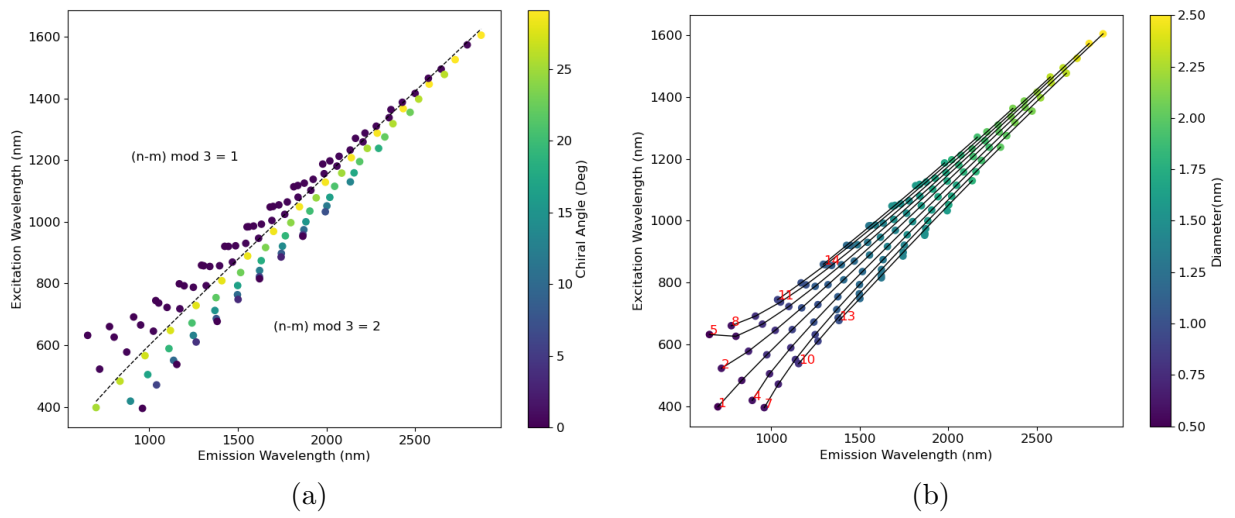


Figure 3.11: Group characteristics of CNTs colored by (a)chiral angle and (b)diameter

Chapter 4

Optical Excitation of Semiconductor Nanoparticles in Hollow-Core Fiber

4.1 Bandgap Overlap

Table shows all hollow-core fiber types available from ThorLabs and the central operating wavelengths for air-filled and D2O-filled fibers. The “air” range can be used for fibers that are selectively core-filled with D2O. The ranges for HC1550 and HC800B are approximated from spectrum measurements and HC2000 and HC1060 are taken from ThorLabs datasheets. The D2O central wavelengths are calculated using the band-gap shift equation

HCPCF	λ_{AIR} (nm)	λ_{D_2O} (nm)	Range (nm)
HC2000	2000	1144	250
HC1550	1550	887	500
HC1060	1060	606	100
HC800B	800	457	200

Table 4.1: Thorlabs fiber bandgap shift.

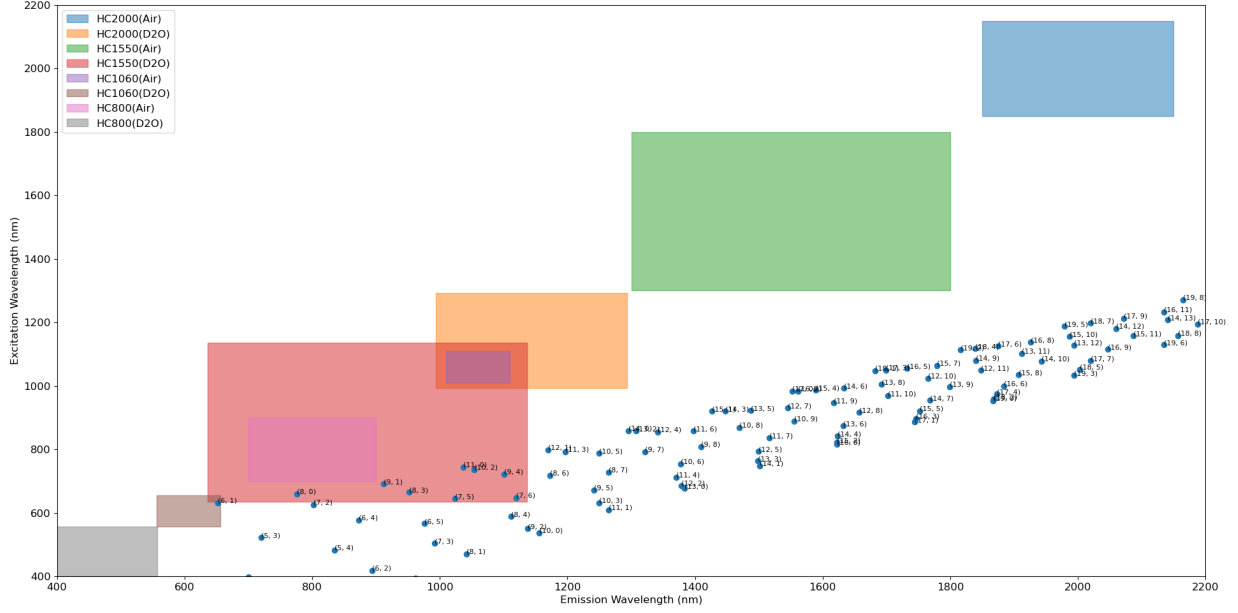


Figure 4.1: Hollow-core fiber bandgap overlayed on CNT emission vs. excitation wavelengths

(n, m)	dt (nm)	Θ (deg)	λ_{11} (nm)	λ_{22} (nm)
(6, 1)	0.52	0.13	652.62	631.79
(7, 2)	0.65	0.21	802.05	625.92
(7, 5)	0.83	0.43	1023.74	645.33
(7, 6)	0.89	27.46	1119.76	647.64
(8, 0)	0.64	0	776.01	660.25
(8, 3)	0.78	0.27	951.61	665.39
(9, 1)	0.76	0.09	912.1	691.29
(9, 4)	0.92	0.31	1100.63	722.39
(10, 2)	0.88	0.16	1053.43	736.68
(11, 0)	0.87	0	1036.93	744.57

Table 4.2: CNTs with emission and excitation transmittable through HC1550 filled with D₂O.

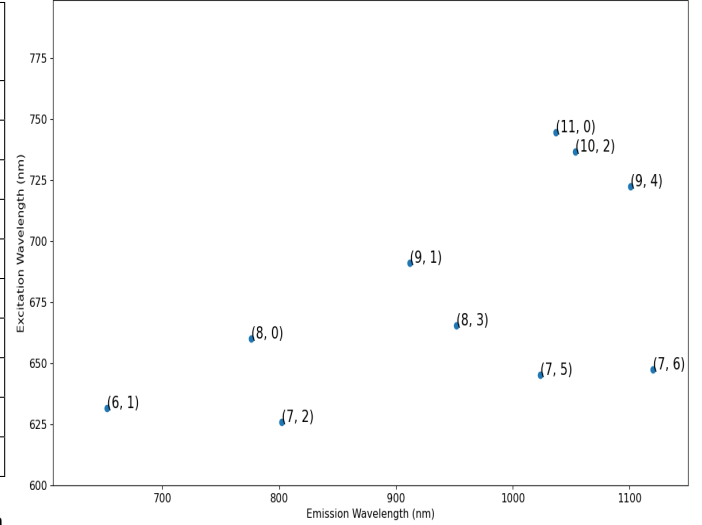


Figure 4.2: 1550HC CNTs

4.1.1 Particle-Mode Interaction and Optical Depth

Optical depth (OD) is a measurement of the opacity of a system, related to the transmitted intensity by $T = \exp(-OD)$. With particles distributed throughout the fiber, the interaction between the beam and particles inside the fiber need to be taken into account. Similar considerations have been calculated for gas-filled HCPCF in cold-atom experiments [25, 26].

Beginning with a single particle interacting with the mode function of a waveguide, the strength of the particle interaction will depend on its position within the mode [27, 28]. The effective mode area of the waveguide is then relevant only in relation to the position of the particle.

$$\sigma_M = \frac{\int dx dy |f_k(x, y)|^2}{|f_k(x_p, y_p)|^2} \quad (4.1)$$

where $f_k(x, y)$ is the transverse mode function and $f(x_p, y_p)$ is the position of the particle. In the case of a Gaussian mode function (as would be in a HCPCF), the photon interaction with the particle will be stronger in the center of the mode and weak at the edges. The optical depth (OD) for a single particle the ratio of the scattering cross-section to that of the effective mode-area $OD = \frac{\sigma_0}{\sigma_M}$, so to find the optical depth over the entire ensemble the product of the number density of the sample and optical depth of each emitter is integrated over the volume :

$$OD_{fiber} = \int_0^{L'} \int_0^{r'} n(r, z) OD(2\pi r) dr dz \quad (4.2)$$

where r' and L' represent the radius and length of the ensemble. While the fibers are fully liquid cladding and core, due to the low interaction and guidance of photons in the PC structure an approximation is made constricting the mode function strictly to the core. This simplifies the dimensions of the integration to just be the radius and length of the fiber. This assumes that the particulates outside of the core do not have a significant contribution. If the distribution of molecules is take to be uniform along the fiber length and radius of the core, then the number density will be:

$$n(r, z) = \frac{N_{particle}}{V_{fiber}} = \frac{N_{particle}}{\pi r_{core}^2 L_{fiber}} \quad (4.3)$$

The integral will simplify to

$$\begin{aligned} OD_{fiber} &= \int_0^{L_{fiber}} \int_0^{r_{core}} n(r_{core}, L_{fiber}) \sigma_0 \frac{2}{\pi w_0^2} e^{-\frac{2r^2}{w_0^2}} (2\pi r) dr dz \\ &= N_{particle} \frac{\sigma_0}{\pi r_{core}^2} \left(1 - e^{-\frac{2r_{core}^2}{w_0^2}}\right) \end{aligned} \quad (4.4)$$

4.2 Indocyanine Green

Due to the difficulty in isolating single-chirality solutions of CNTs, as outlined in the previous chapter, indocyanine green (ICG) - a fluorescent dye often used in microscopy imaging[36, 37] - was initially used in place of CNTs in the fiber. This particular dye is an organic semiconductor with HOMO-LUMO gap calculations estimating a 2eV energy gap, with variations depending on the solvent[29]. The HOMO and LUMO energy levels in organic semiconductors are parallel to the maximum valence and minimum conduction, and the aforementioned energy gap falls within the range of energy bandgaps found in inorganic semiconductors.

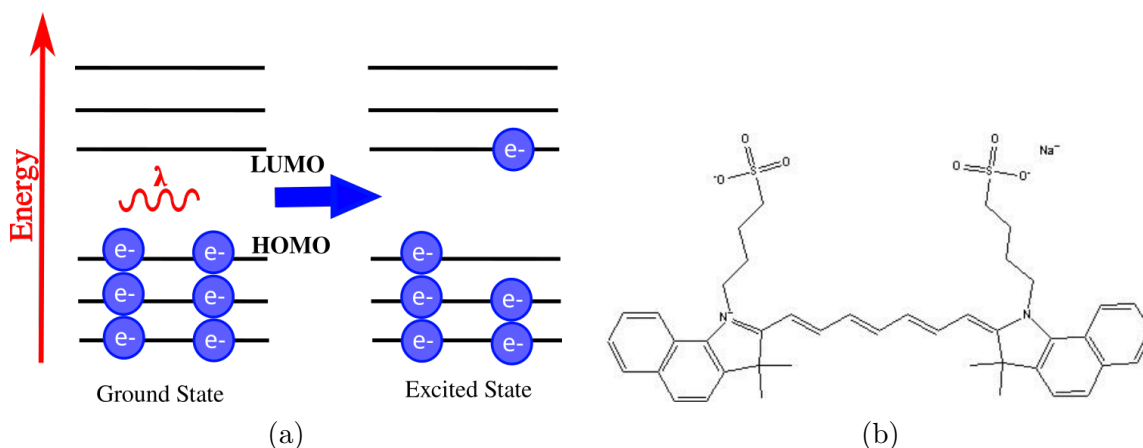


Figure 4.3: (a) Depiction of the HOMO-LUMO gap in organic semiconductors and the transition occurring between ground and excited states. (b) The chemical structure of ICG provided by MP Biomedicals.

The following section details the the optical properties of ICG and measurements of the optical properties when confined in HCPCF.

Absorption Cross-Section

ICG absorbs wavelengths between 600-900nm. The absorption is largely bimodal, with the greatest excitation occurring at 780nm and 700nm, but transforms into a monomeric distribution at 780nm at low concentrations and 700nm at high concentrations. Due to

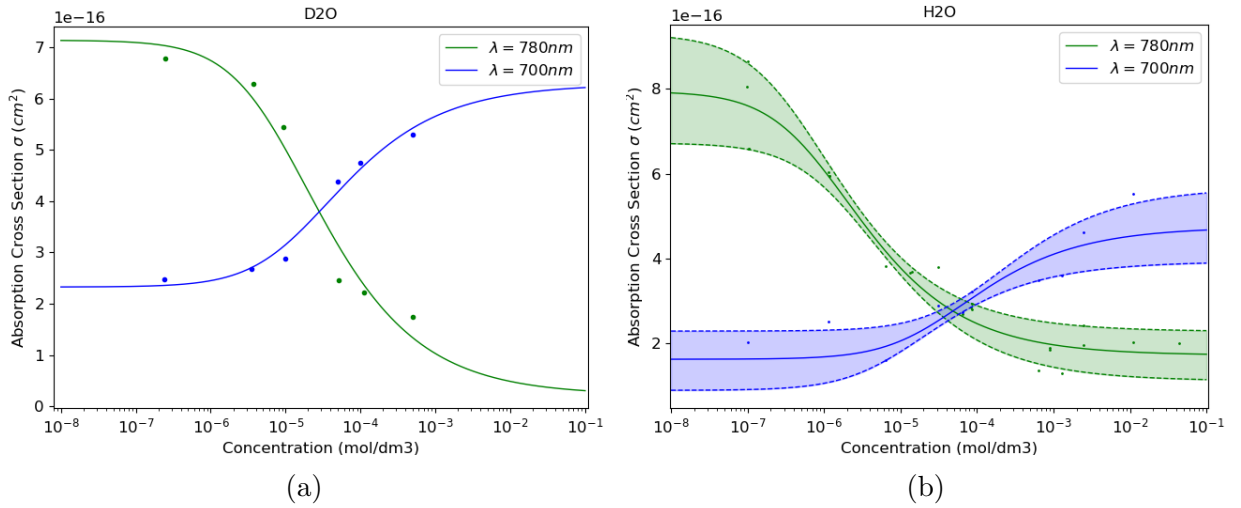


Figure 4.4: Absorption cross-section at peak wavelengths 700nm(blue) and 780nm(green) for ICG dissolved in D2O(a) and H2O(b) . Data from (cite) was fitted using a linear regression model.

the chemical formation of ICG, the absorption of the molecule when dissolved in a solvent is highly concentration-dependent. ICG is made up of monomers, which are a type of molecule that can react with other monomers to form polymer chains. In the case of ICG, its monomers react with each other to form dimers, a chain of two join monomers. With higher concentrations, monomers are closer in proximity and the molecules are more likely shift from monomers to dimers which are less likely to be excited and shift the center absorption wavelength. The concentration of monomer M to dimmers D is governed by the equilibrium reaction



and law of mass action relation concentration

$$[D] = K_D[M]^2 \quad (4.6)$$

Where K_D is the dimmerization constant . Written in terms of concentration C and mole fractions, $[M] = x_M C = (1 - x_D)C$ and $[D] = \frac{x_D}{2}C$., the mole fraction of dimmers can be written in terms of the dimmerization constant and concentration.

$$x_D = 1 + \frac{1}{4K_D C} - \sqrt{\left(1 + \frac{1}{4K_D C}\right)^2 - 1} \quad (4.7)$$

The absorption cross-section model for ICG[32, 34] will be an average of the affects of the of monomers and dimmers, where σ_M and σ_D are the monomer and dimer absorption cross-sections respectively.

$$\sigma = x_M \sigma_M + x_D \sigma_D = \sigma_M - x_D(\sigma_M - \sigma_D) \quad (4.8)$$

Plugging (4.7) into (4.8), remaining parameters could be found by doing a linear regression fit to absorption cross-section vs. concentration data from literature and the expected absorption cross-section could be calculated for any concentration. For ICG dissolved in H2O, the existing literature has some variation and so the upper/lower bounds and average were taken, while little data was available for ICG dissolved in D2O. The behavior in H2O and D2O are quite similar and are plotted in Fig4.4. At lower concentrations the absorption cross-section is slightly greater for D2O than H2O, with the reverse for high concentrations.

$\lambda_{peak} = 780nm$	K_D	σ_M	σ_D
[30]	$6.01x10^5$	$9.29x10^{-16}$	$2.28x10^{-16}$
[31]	$1.03x10^5$	$6.74x10^{-16}$	$1.54x10^{-16}$
[32]	$1.40x10^5$	$6.72x10^{-16}$	$1.11x10^{-16}$
Average	$3.06x10^6$	$7.94x10^{-16}$	$1.72x10^{-16}$

Table 4.3: Absorption Cross Section parameter fitting of ICG dissolved in deionized water. Fitting done with linear regression on σ vs. concentration data measured at $\lambda = 780nm$ from literature.

$\lambda_{peak} = 700nm$	K_D	σ_M	σ_D
[30]	$3.00x10^3$	$2.29x10^{-16}$	$25.68x10^{-16}$
[32]	$3.06x10^4$	$8.89x10^{-16}$	$3.93x10^{-16}$
Average	$9.31x10^3$	$1.62x10^{-16}$	$4.74x10^{-16}$

Table 4.4: Absorption Cross Section parameter fitting of ICG dissolved in deionized water. Fitting done with linear regression on σ vs. concentration data at $\lambda = 700nm$ from literature.

λ_{peak}	K_D	σ_M	σ_D
$780nm$	$3.22x10^4$	$7.14x10^{-16}$	$2.68x10^{-17}$
$700nm$	$1.67x10^4$	$2.833x10^{-16}$	$6.28x10^{-16}$

Table 4.5: Absorption Cross Section parameter fitting of ICG dissolved in heavy water. Fitting done with linear regression on σ vs. concentration data at $\lambda = 700nm$ from literature.

Photostability

At high concentrations, ICG behaves as a "J-aggregate", a category of dyes that have a shift in absorption band to larger wavelengths in certain solvents. When mixed into water and other solvents, ICG shifts over time to a center wavelength of 893nm. This process can be accelerated under high heat in high-concentration (in the range of 1000ppm solutions) forms [33], J-aggregates can be stored at room temperature for several months. However, at such a state the dye will be too optically dense to observe any optical excitation and when diluted to perform such measurements, the J-aggregates will begin to detach into smaller molecules within 24hrs. The effects of dye concentration of storage life in aqueous solutions becomes a tricky balance at single-digit ppm concentrations, where the fluorescence intensity of the dye is at its greatest but with degradation to undetectable levels occurring in a couple of hours at best if in optimal storage conditions[31, 35]. The rate of deterioration occurs so linearly based on the initial concentration of ICG[30], but the amount of light exposure of the solution will also exasperate the degradation rate[35].

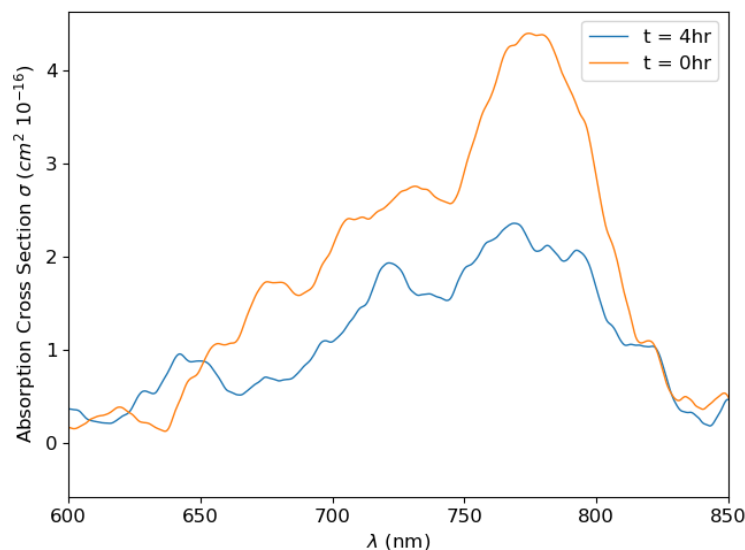


Figure 4.5: Degradation of a 4.5ppm initial concentration sample after 4hrs of light exposure reduced to a 2ppm concentration.

Fluorescence

Photoluminescence in the dye is emitted in the range of 750-900nm. overlapping with the absorption spectrum. The peak emission wavelength for ICG varies within 800nm-820nm[34, 35] when excited at 780nm and decreases as solution concentration increases, The dimmerization effects are attributed to (a) The formation of weakly fluorescent ICG molecular aggregates at high concentrations (b) self-quenching and (c) re-absorption of the emitted fluorescence by the ICG molecules due to overlap of the absorption and emission spectra. In the J-aggregate form the excitation wavelength shifts to 834nm and the emission peak at 890nm, however, low quantum yield and strong light scattering does not lend to accurate measurements[33].

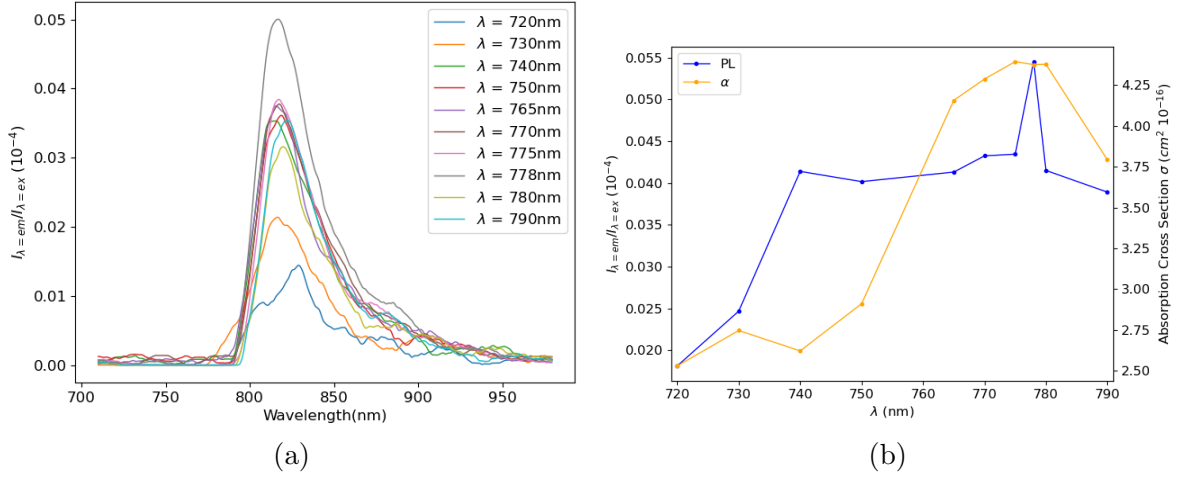


Figure 4.6: (a) Fluorescence spectrum of 4.5ppm sample (b) Maximum fluorescence and maximum absorption spectrum of 4.5ppm initial concentration sample

4.2.1 Experiment Set-Up

Preparation 1. Stock 1) Using the micropipette, measure 1ml of D₂O or H₂O into a vial 2) Using the scale, measure 1mg of ICG powder 3) Pour the measured ICG into the 1ml of D₂O/H₂O 4) Close the vial and shake for 15 seconds to dissolve
2. Dilution 1) Measure 5ml of D₂O or H₂O into a vial 2) Using the pipette, measure 10ul of the stock solution 3) Output the 10ul of stock solutions into the 100ml of D₂O/H₂O 4) Close the vial and shake for 15 seconds to dissolve Used within 12 hrs of creation

4.2.2 ICG in HCPCF

Low-concentration samples of dye were prepared and filled a 800nm HCPCF core and 1550nm HCPCF core and cladding. The absorption spectrum of the dye was detected, though muddled by additional losses from the fiber, as shown in Fig. 4.7. Additionally, there is an observed 18nm shift in the peak absorption from 778nm to 796nm in the 1550nm bandgap-shifted liquid-filled fiber, while the 800nm liquid-core fiber has an insignificant 4nm shift in peak from 775nm to 771nm.

For 800nm core-filled HCPCF, ICG solutions were prepared with H_2O and D_2O solvents,

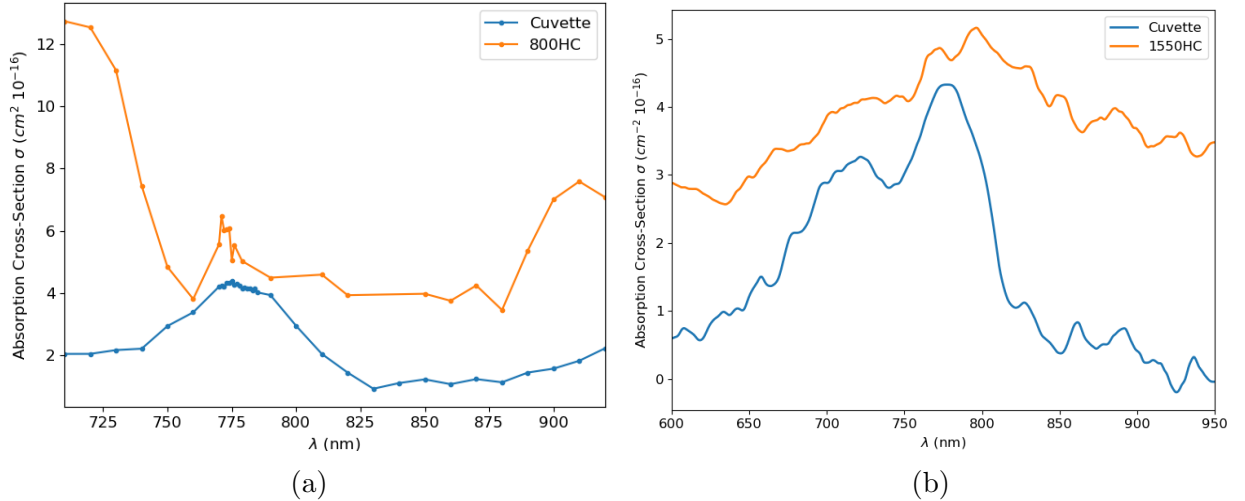


Figure 4.7: Absorption spectrum of ICG samples (a) 2.5 ppm concentration in core of 800nm HCPCF and (b) 4 ppm concentration in core and cladding of 1550nm HCPCF.

but fluorescence was only guided in the D_2O . In the 800HC fiber there is already significant loss coming from the narrow bandgap in combination with lower refractive index contrast

of using a liquid medium, as half of the absorption spectrum is outside the bandgap; it is suspected that the absorption of effects of H_2O in the NIR (discussed in chapter 2) and re-absorption from the overlapping excitation-emission spectra was greater than the number of emitted photons. The fluorescence guided in the 800nm HCPCF is also influenced by the bandgap, shown in 4.9b, the emission has a large shifts in peak for excitation between 745 – 775nm - wavelengths at the edge of the bandgap and with high absorption effects- varying peak fluorescence between 800 – 820nm while for excitation above 775nm the fluorescence stays centered at 805nm.

Fluorescence was also detected in ICG-filled 1550nm HCPCF with D_2O as the solvent and had the best ratio of fluorescence intensity to emission intensity ("fraction of fluorescence"). For a 4ppm ICG sample the fraction of fluorescence are compared in Fig. 4.8 for excitation wavelengths below the emission wavelength range. The peak fluorescence in the cuvette was at 820nm but is shifted down 10nm to 810nm in the fiber and the fraction of fluorescence in 1550nm HCPCF $\sim 35x$ greater than that measured through the cuvette. For the 3.7ppm sample in 800nm HCPCF measured similar fraction of fluorescence to the cuvette sample at the excitation wavelength of peak absorption(778nm), but the exact source of the large difference in fraction of fluorescence in the 1550nm and 800nm HCPCF/cuvette are not clear.

At the maximum absorption wavelength, measurements of the the fraction of fluorescence and output power at the excitation wavelength are . Overall, the collection efficiency is in the range of 0.001%, for milliwatts of pump power nanowatts of power at the emission frequency.

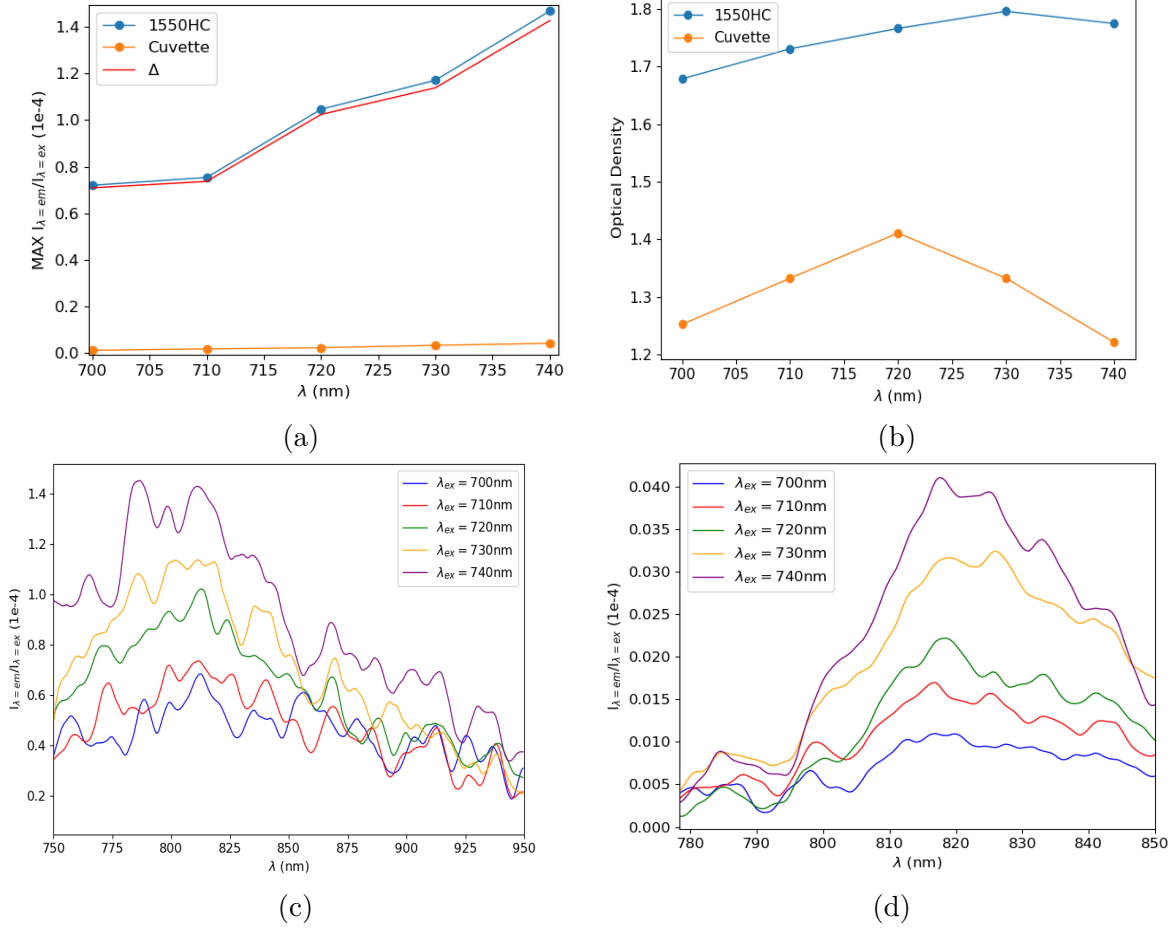


Figure 4.8: (a) The maximum fraction of fluorescence is plotted against excitation wavelength for a 4ppm ICG sample in a 1cm piece of 1550nm HCPCF and 1cm cuvette. The maximum fraction of fluorescence of the ICG in the cuvette is only 4% of that measured in fiber. (b) The optical density at each excitation wavelength. The fraction of fluorescence spectrum of the 4ppm ICG solution in (c) 1550nm HCPCF (d) a cuvette.

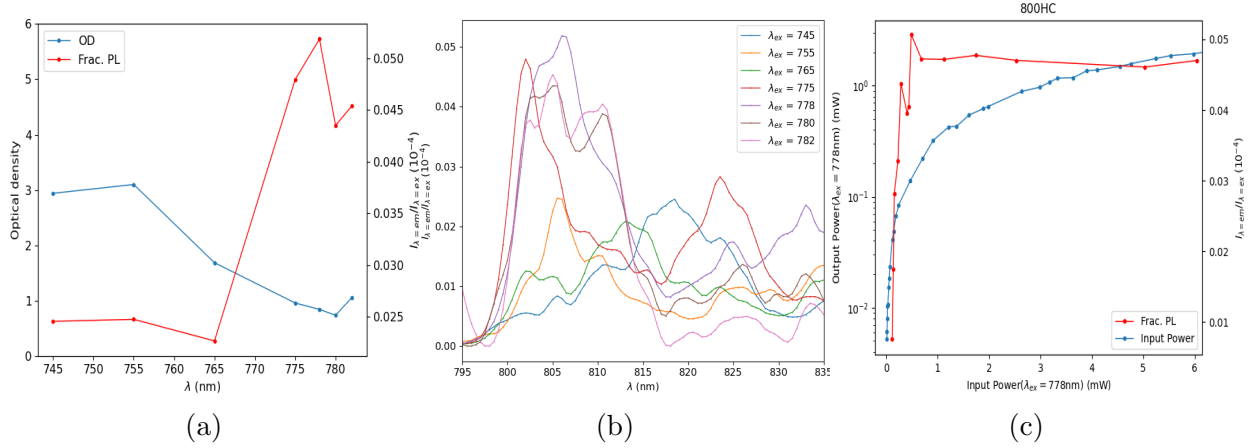


Figure 4.9: Measurements of 3.7ppm ICG sample in a 2cm piece of core-filled 800nm HCPCF (a) The maximum fraction of fluorescence and optical density against excitation wavelength. (b) The fraction of fluorescence spectrum (c) Measured output peak power and fractional fluorescence as a function of input power.

Optical Density Calculations

For calculations of optical density within the HCPCF, the core radius will be $r_{core} = 5 \pm 0.05\mu m$ with beam waist $w_0 = 4.5 \pm 0.05\mu m$ for 1550nm HCPCF and $r_{core} = 3.75 \pm 0.05\mu m$ with beam waist $w_0 = 2.75 \pm 0.05$. For ICG dispersed in water, molecule aggregate radii have been measured between $2nm - 200nm$ [38] with J-aggregates forming at radii $> 50nm$ [39]. Due to the low concentration samples of dye used in our experiments, the lower range of molecule diameter is used, meeting the Raleigh scattering approximation condition $\frac{2\pi r}{\lambda} \ll 1$, the scattering cross-section is

$$\sigma_0 = \frac{2\pi^5(2r_{particle})^6}{3\lambda^4} \left(\frac{N^2 - 1}{N^2 + 2} \right)^2 \quad (4.9)$$

where $N = \frac{n_{particle}}{n_{solvent}}$. Applying the parameters above and (4.9) to (4.4) the estimated concentration of ICG molecules for optically dense medium ($OD_{fiber} = 1$) has a range of $N_{particle} = 1.5 \times 10^8 \sim 2.0 \times 10^{14}$ molecules and $N_{particle} = 8.2 \times 10^7 \sim 1.1 \times 10^{14}$ molecules for 1550nm and 800nm HCPCF respectively varying the ICG aggregate radii within the approximation condition.

For the $L_{fiber} = 1cm$ piece of fiber, the number of molecules contained in a perfectly filled core will be

$$N_{particle} = M_{ICG} * C * V_{fiber} = \frac{1mol}{774.98g} * \frac{4mg}{1dm^3} * \pi(5\mu m)^2(1cm) = 2.441 \times 10^9 molecules \quad (4.10)$$

Using the measured optical density in the fiber, Fig. 4.8b the estimated radius of the aggregate ICG molecules is $r_{particle} = 13.7 \pm 0.2nm$.

Chapter 5

Conclusion

5.0.1 Experimental Outcomes

Determined the bandgap of liquid-filled fibers of H_2O and D_2O Measured the interaction of suspended ICG particles with the mode of the fiber results show the potential of creating a fluorescent light source with liquid core fibers

CNTs

CNT samples from QuIN lab measured absorption of selectively sorted sample no fluorescence - need to do concentration-based experiemnts furthure with nonsorted CNT sample in D2O

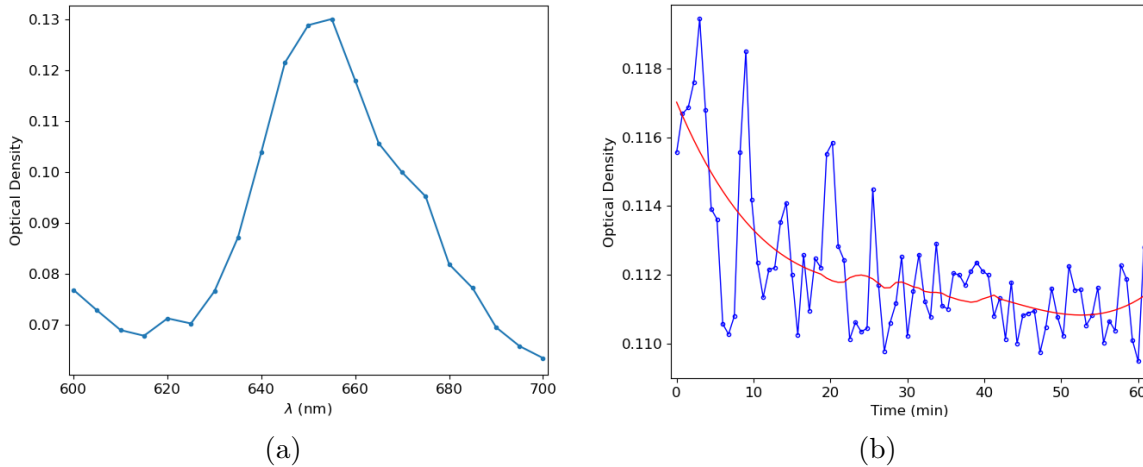


Figure 5.1: (a) (b)

5.1 ECDL

what is ECDL fiber-integration diagram advantages

References

- [1] Yariv, Amnon and Pochi Albert Yeh, *Optical Waves in Crystals: Propagation and Control of Laser Radiation*, 1st ed. Wiley-Interscience, 2002.
- [2] J. D. Joannopoulos, *Photonic crystals: molding the flow of light*, 2nd ed. Princeton: Princeton University Press, 2008.
- [3] P. R. Villeneuve and M. Piché, “Photonic band gaps in two-dimensional square and hexagonal lattices,” *Phys. Rev. B*, vol. 46, no. 8, pp. 4969–4972, Aug. 1992, doi: 10.1103/PhysRevB.46.4969.
- [4] I. A. Sukhoivanov and I. V. Guryev, *Photonic Crystals: Physics and Practical Modeling*, vol. 152. Berlin, Heidelberg: Springer Berlin Heidelberg, 2009. doi: 10.1007/978-3-642-02646-1.
- [5] T. A. Birks, D. M. Bird, T. D. Hedley, J. M. Pottage, and P. St. J. Russell, “Scaling laws and vector effects in bandgap-guiding fibres,” *Opt. Express*, vol. 12, no. 1, p. 69, 2004, doi: 10.1364/OPEX.12.000069.
- [6] G. Antonopoulos, F. Benabid, T. A. Birks, D. M. Bird, J. C. Knight, and P. St. J. Russell, “Experimental demonstration of the frequency shift of bandgaps in photonic crystal fibers due to refractive index scaling,” *Opt. Express*, vol. 14, no. 7, p. 3000, 2006, doi: 10.1364/OE.14.003000.
- [7] G. Antonopoulos, F. Benabid, T. A. Birks, D. M. Bird, J. C. Knight, and P. St. J. Russell, “Experimental demonstration of the frequency shift of bandgaps in photonic crystal fibers due to refractive index scaling,” *Opt. Express*, vol. 14, no. 7, p. 3000, 2006.
- [8] R. A. Maruf and M. Bajcsy, “On-chip splicer for coupling light between photonic crystal and solid-core fibers,” *Appl. Opt.*, vol. 56, no. 16, p. 4680, Jun. 2017.

- [9] L. Xiao, W. Jin, M. S. Demokan, H. L. Ho, Y. L. Hoo, and C. Zhao, “Fabrication of selective injection microstructured optical fibers with a conventional fusion splicer,” *Opt. Express*, vol. 13, no. 22, p. 9014, 2005.
- [10] S. Kedenburg, M. Vieweg, T. Gissibl, and H. Giessen, “Linear refractive index and absorption measurements of nonlinear optical liquids in the visible and near-infrared spectral region,” *Opt. Mater. Express*, vol. 2, no. 11, p. 1588, Nov. 201
- [11] S. Dresselhaus, “PHYSICS OF CARBON NANOTUBES,” *Carbon*, 33(7), 883-891, 1995.
- [12] V. Popov, “Carbon nanotubes: properties and application,” *Materials Science and Engineering: R: Reports*, vol. 43, no. 3, pp. 61–102, Jan. 2004.
- [13] S. Yamashita, “Nonlinear optics in carbon nanotube, graphene, and related 2D materials,” *APL Photonics*, vol. 4, no. 3, p. 034301, Mar. 2019.
- [14] R. Saito, M. Fujita, G. Dresselhaus, and M. S. Dresselhaus, “Electronic structure of chiral graphene tubules,” *Appl. Phys. Lett.*, vol. 60, no. 18, pp. 2204–2206, May 1992.
- [15] C. Thomsen, S. Reich, and J. Maultzsch, *Carbon Nanotubes: Basic Concepts and Physical Properties*, 1st ed. Wiley, 2004.
- [16] H. Kataura et al., “Optical properties of single-wall carbon nanotubes,” *Synthetic Metals*, vol. 103, no. 1–3, pp. 2555–2558, Jun. 1999.
- [17] S. Yamashita, “A Tutorial on Nonlinear Photonic Applications of Carbon Nanotube and Graphene,” *J. Lightwave Technol.*, vol. 30, no. 4, pp. 427–447, Feb. 2012.
- [18] A. Gambetta et al., “Sub-100 fs two-color pump-probe spectroscopy of Single Wall Carbon Nanotubes with a 100 MHz Er-fiber laser system,” p. 8, 2008.
- [19] R. B. Weisman and S. M. Bachilo, “Dependence of Optical Transition Energies on Structure for Single-Walled Carbon Nanotubes in Aqueous Suspension: An Empirical Kataura Plot,” *Nano Lett.*, vol. 3, no. 9, pp. 1235–1238, Sep. 2003.
- [20] S. M. Bachilo, M. S. Strano, C. Kittrell, R. H. Hauge, R. E. Smalley, and R. B. Weisman, “Structure-Assigned Optical Spectra of Single-Walled Carbon Nanotubes,” *Science*, vol. 298, no. 5602, pp. 2361–2366, Dec. 2002.

- [21] S. Giordani et al., “Debundling of Single-Walled Nanotubes by Dilution: Observation of Large Populations of Individual Nanotubes in Amide Solvent Dispersions,” *J. Phys. Chem. B*, vol. 110, no. 32, pp. 15708–15718, Aug. 2006.
- [22] A. Martinez and S. Yamashita, “Carbon Nanotube-Based Photonic Devices: Applications in Nonlinear Optics,” In: J. M. Marulanda, Ed., *Carbon Nanotubes Applications on Electron Devices*, InTech, 2011.
- [23] V. A. Margulis and T. A. Sizikova, “Theoretical study of third-order nonlinear optical response of semiconductor carbon nanotubes,” *Physica B: Condensed Matter*, vol. 245, no. 2, pp. 173–189, Mar. 1998.
- [24] E. Turek, T. Shiraki, T. Shiraishi, T. Shiga, T. Fujigaya, and D. Janas, “Single-step isolation of carbon nanotubes with narrow-band light emission characteristics,” *Sci Rep*, vol. 9, no. 1, p. 535, Dec. 2019.
- [25] M. Bajcsy et al., “Laser-cooled atoms inside a hollow-core photonic-crystal fiber,” *Phys. Rev. A*, vol. 83, no. 6, p. 063830, Jun. 2011, doi: 10.1103/PhysRevA.83.063830.
- [26] A. P. Hilton, C. Perrella, F. Benabid, B. M. Sparkes, A. N. Luiten, and P. S. Light, “High-efficiency cold-atom transport into a waveguide trap,” *Phys. Rev. Applied*, vol. 10, no. 4, p. 044034, Oct. 2018, doi: 10.1103/PhysRevApplied.10.044034.
- [27] P. Domokos, P. Horak, and H. Ritsch, “Quantum description of light-pulse scattering on a single atom in waveguides,” *Phys. Rev. A*, vol. 65, no. 3, p. 033832, Mar. 2002, doi: 10.1103/PhysRevA.65.033832.
- [28] M. T. Manzoni, “New Systems for Quantum Nonlinear Optics,” 2017, Thesis, p. 39-40.
- [29] X. Fang et al., “One-step condensation synthesis and characterizations of indocyanine green,” *Results in Chemistry*, vol. 3, p. 100092, Jan. 2021, doi: 10.1016/j.rechem.2020.100092.
- [30] W. Holzer et al., “Photostability and thermal stability of indocyanine green,” *Journal of Photochemistry and Photobiology B: Biology*, vol. 47, no. 2-3, pp. 155-164, Dec. 1998.
- [31] M. L. Landsman, G. Kwant, G. A. Mook, and W. G. Zijlstra, “Light-absorbing properties, stability, and spectral stabilization of indocyanine green,” *Journal of Applied Physiology*, vol. 40, no. 4, pp. 575–583, Apr. 1976.

- [32] M. Mauerer, A. Penzkofer, and J. Zweck, “Dimerization, J-aggregation and J-disaggregation dynamics of indocyanine green in heavy water,” *Journal of Photochemistry and Photobiology B: Biology*, vol. 47, no. 1, pp. 68–73, Nov. 1998.
- [33] F. Rotermund, R. Weigand, W. Holzer, M. Wittmann, and A. Penzkofer, “Fluorescence spectroscopic analysis of indocyanine green J aggregates in water,” *Journal of Photochemistry and Photobiology A: Chemistry*, vol. 110, no. 1, pp. 75–78, Oct. 1997.
- [34] R. Philip, A. Penzkofer, W. Bäuml, R. M. Szeimies, and C. Abels, “Absorption and fluorescence spectroscopic investigation of indocyanine green,” *Journal of Photochemistry and Photobiology A: Chemistry*, vol. 96, no. 1–3, pp. 137–148, May 1996.
- [35] V. Saxena, M. Sadoqi, and J. Shao, “Degradation Kinetics of Indocyanine Green in Aqueous Solution,” *Journal of Pharmaceutical Sciences*, vol. 92, no. 10, pp. 2090–2097, Oct. 2003.
- [36] D. Farrakhova et al., “Fluorescence imaging analysis of distribution of indocyanine green in molecular and nanoform in tumor model,” *Photodiagnosis and Photodynamic Therapy*, vol. 37, p. 102636, Mar. 2022, doi: 10.1016/j.pdpdt.2021.102636.
- [37] E. Spartalis et al., “Intraoperative Indocyanine Green (ICG) Angiography for the Identification of the Parathyroid Glands: Current Evidence and Future Perspectives,” *In Vivo*, vol. 34, no. 1, pp. 23–32, 2020, doi: 10.21873/invivo.11741.
- [38] D. J. DeDora et al., “Sulfobutyl ether β -cyclodextrin and methyl β -cyclodextrin enhance and stabilize fluorescence of aqueous indocyanine green: Sulfobutyl Ether β -Cyclodextrin and METHYL β -Cyclodextrin,” *J. Biomed. Mater. Res.*, vol. 104, no. 7, pp. 1457–1464, Oct. 2016, doi: 10.1002/jbm.b.33496.
- [39] R. Weigand, F. Rotermund, and A. Penzkofer, “Degree of aggregation of indocyanine green in aqueous solutions determined by Mie scattering,” *Chemical Physics*, vol. 220, no. 3, pp. 373–384, Aug. 1997, doi: 10.1016/S0301-0104(97)00150-X.

APPENDICES

.1 CNT Sample Preparation

- Sample history 1) SG65i powder purchased from Sigma Aldrich 2) Dispersed in a surfactant 3) Purification steps 4) Sorting with polymers & surfactants 5) Polymer exchange 6) UV-vis measurements -. (7,5), (7,6) dominant: 65 % in the sample -. Semiconducting: 99 %
- Sample Condition -. SWCNTs are in DI water with DOC 0.04% -. Greenish color -. Amount: 1 mL

Glossary

This document is incomplete. The external file associated with the glossary ‘main’ (which should be called `uw-ethesis.gls`) hasn’t been created.

Check the contents of the file `uw-ethesis.glo`. If it’s empty, that means you haven’t indexed any of your entries in this glossary (using commands like `\gls` or `\glsadd`) so this list can’t be generated. If the file isn’t empty, the document build process hasn’t been completed.

You may need to rerun \LaTeX . If you already have, it may be that \TeX ’s shell escape doesn’t allow you to run `makeindex`. Check the transcript file `uw-ethesis.log`. If the shell escape is disabled, try one of the following:

- Run the external (Lua) application:
`makeglossaries-lite "uw-ethesis"`
- Run the external (Perl) application:
`makeglossaries "uw-ethesis"`

Then rerun \LaTeX on this document.

This message will be removed once the problem has been fixed.

Abbreviations

This document is incomplete. The external file associated with the glossary ‘abbreviations’ (which should be called `uw-ethesis.gls-abr`) hasn’t been created.

Check the contents of the file `uw-ethesis.glo-abr`. If it’s empty, that means you haven’t indexed any of your entries in this glossary (using commands like `\gls` or `\glsadd`) so this list can’t be generated. If the file isn’t empty, the document build process hasn’t been completed.

You may need to rerun \LaTeX . If you already have, it may be that \TeX ’s shell escape doesn’t allow you to run `makeindex`. Check the transcript file `uw-ethesis.log`. If the shell escape is disabled, try one of the following:

- Run the external (Lua) application:
`makeglossaries-lite "uw-ethesis"`
- Run the external (Perl) application:
`makeglossaries "uw-ethesis"`

Then rerun \LaTeX on this document.

This message will be removed once the problem has been fixed.

Nomenclature

This document is incomplete. The external file associated with the glossary ‘nomenclature’ (which should be called `uw-ethesis.nomenclature-gls`) hasn’t been created.

Check the contents of the file `uw-ethesis.nomenclature-glo`. If it’s empty, that means you haven’t indexed any of your entries in this glossary (using commands like `\gls` or `\glsadd`) so this list can’t be generated. If the file isn’t empty, the document build process hasn’t been completed.

You may need to rerun \LaTeX . If you already have, it may be that \TeX ’s shell escape doesn’t allow you to run `makeindex`. Check the transcript file `uw-ethesis.log`. If the shell escape is disabled, try one of the following:

- Run the external (Lua) application:
`makeglossaries-lite "uw-ethesis"`
- Run the external (Perl) application:
`makeglossaries "uw-ethesis"`

Then rerun \LaTeX on this document.

This message will be removed once the problem has been fixed.

List of Symbols

This document is incomplete. The external file associated with the glossary ‘symbols’ (which should be called `uw-ethesis.symbols-gls`) hasn’t been created.

Check the contents of the file `uw-ethesis.symbols-glo`. If it’s empty, that means you haven’t indexed any of your entries in this glossary (using commands like `\gls` or `\glsadd`) so this list can’t be generated. If the file isn’t empty, the document build process hasn’t been completed.

You may need to rerun \LaTeX . If you already have, it may be that \TeX ’s shell escape doesn’t allow you to run `makeindex`. Check the transcript file `uw-ethesis.log`. If the shell escape is disabled, try one of the following:

- Run the external (Lua) application:
`makeglossaries-lite "uw-ethesis"`
- Run the external (Perl) application:
`makeglossaries "uw-ethesis"`

Then rerun \LaTeX on this document.

This message will be removed once the problem has been fixed.